Universität Hamburg

Commissioning of an LED Calibration & Monitoring System for the Prototype of a Hadronic Calorimeter

Diplomarbeit
von
Nanda Wattimena

Institut für Experimentalphysik
Universität Hamburg
April 2006

Abstract

The anticipated physics program for the *International Linear Collider* (ILC) requires a highly granular hadronic calorimeter. One option for such a tracking calorimeter is a scintillator-steel sandwich structure placed inside the magnetic coil. The development of hadronic showers will be studied with a physics prototype, in order to improve current models. This prototype, currently being built within the collaboration for a *CAlorimeter for the LInear Collider Experiment* (CALICE) at the *Deutsches Elektronen-Synchrotron* (DESY) also serves to test a new semiconductor based photodetector the so called silicon photomultiplier.

The calibration of these new photodetectors requires to take into account their nonlinear response.The response function, describing this behaviour, is investigated in this thesis. A calibration and monitoring system, needed to correct for the temperature and voltage dependence of the silicon photomultiplier signals and to observe changes of their response over time, is optimised and tested.

Zusammenfassung

Um das angestrebte physikalische Program am *International Linear Collider* (ILC) zu erfüllen, muss das dort verwendete hadronische Kalorimeter eine sehr hohe Ortsauflösung haben. Dies kann mit einem Spurkalorimeter in Szintillator-Stahl-Schichtstruktur, das innerhalb des Magnetfeldes angeordnet ist, realisiert werden. Um die Entwicklung hadronischer Schauer zu untersuchen und aktuelle Modelle zu verbessern, wird ein Prototyp eines solchen Kalorimeters in der Kollaboration für ein *CAlorimeter for the LInear Collider Experiment* (CALICE) am Forchungszentrum *Deutsches Elektronen-Synchrotron* (DESY) gebaut. Darüber hinaus wird dieser Prototyp auch zur Erprobung eines neuen Halbleiterdetektors, dem Silizium-Sekundärelektronenvervielfacher verwendet.

Im Rahmen dieser Diplomarbeit wird das nichtlineare Ansprechverhalten dieser neuen Sekundärelektronenvervielfacher, das bei ihrer Kalibration berücksichtigt werden muss, untersucht. Zur Korrektur der Temperatur- und Spannungsabhängigkeit des Ausgangssignals der Photodetektoren ist ein Kalibrations- und Überwachungssystem notwendig. Weiterhin wird dieses System, das auch zur Überprüfung der zeitlichen Änderungen des Ansprechverhaltens dient, optimiert und getestet.

Contents

List of Figures

Chapter 1

Introduction

The elementary particles and forces of the world are explored at high energy particle colliders. The observed phenomena are successfully described by the Standard Model of particle physics. This model has been tested at experiments all over the world. But still there is one predicted particle, the light elementary Higgs boson that has not yet been observed at any existing accelerator, because their centre of mass energy is not high enough to produce this particle. From direct searches at running experiments it is known with 95% confidence level that the Higgs mass has to be more than $m_{\mathrm{H}} > 114.4$ GeV. Indirect searches from precision electroweak measurements predict the Standard Model Higgs mass to be $m_{\mathrm{H}} < 207$ GeV [2]. In other scenarios the Higgs can be up to 800 GeV and new particles, e.g. supersymmetric particles, are postulated [3]. To discover and characterise these particles, a new accelerator with higher centre of mass energies is needed. The *Large Hadron Collider* (LHC) that is currently built at the *Conseil Européen pour la Recherche Nucléaire* (CERN) will most probably discover the Higgs boson and the lightest supersymmetric particles, if they exist. Anyhow, an electron-positron collider is necessary for the precise characterisation of these heavy particle.

The *International Linear Collider* (ILC) is designed as a superconducting electron-positron accelerator with a centre of mass energy ranging from 91 GeV, equivalent to the Z boson mass, up to 1 TeV. This energy range will allow for a precise determination of the standard model Higgs boson and other heavy particles. The ILC will also serve for precision tests of the Standard Model, e.g. electroweak symmetry breaking mechanisms, and maybe discover new physics, e.g. supersymmetry.

The precision measurements planned at the ILC require an excellent detector. Presently there are four different designs under investigation: the *Silicon Detector* (SiD) [4]+[5], the *Large Detector Concept* (LDC) [6]+[7], the *Global Large Detector* (GLD) [8]+[9], and the *4th Concept detector* (4th) [10]. The different ongoing research and development (R&D) programs for the various detector concepts in various groups all over the world is discussed in detail in [11].

The calorimeter plays an important role in these detector concepts. The separation of W and Z bosons in multiple jet final states by their invariant mass, as it is necessary in many physics studies, requires a jet energy resolution better than $30\%/\sqrt{E}$ [13].

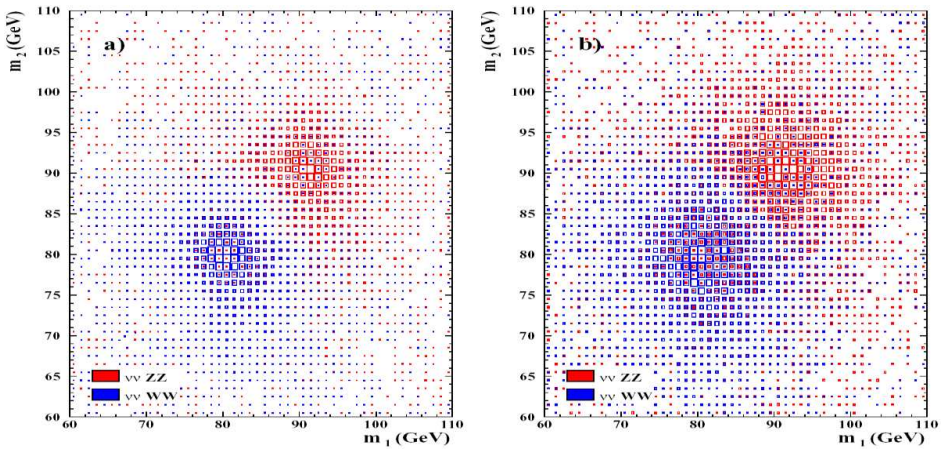

Figure 1.1: Reconstructed masses for $e^+e^- \rightarrow WW\nu\overline{\nu}$ and $e^+e^- \rightarrow ZZ\nu\overline{\nu}$ events for $\sigma_E/E = 30\%/\sqrt{E}$ as proposed for the ILC detector (left) and $\sigma_E/E = 60\%/\sqrt{E}$ as achieved at the LEP experiments (right) [14].

Such a high resolution can be achieved with a calorimeter of high longitudinal and transversal granularity in combination with a new approach for the reconstruction method, which exploits at best the potentiality of each sub-detector. This method is called particle flow concept (see Section 2.1).

One possible realisation of a hadronic calorimeter with high granularity is an analogue sandwich calorimeter with 2 cm steel plates as absorber material and small scintillator tiles as active medium. A 1 m^3 physics prototype using this technology is currently being built at the *Deutsches Elektronen-Synchrotron* (DESY). It will be used to study hadronic shower development with unprecedented precision, due to its high granularity. The scintillator tile size ranges from 3×3 cm^2 in the core, over 6×6 cm^2 to 12×12 cm^2 in the outer regions. They are read-out by a new semiconductor based photodetector, called silicon photomultiplier (SiPM). As the SiPM signal varies with temperature and voltage changes, a monitoring system based on light emitting diodes (LEDs) is necessary.

In this thesis the monitoring system for the physics prototype is described and data taken with a first prototype of the monitoring system is analysed. As the monitoring system should cover the entire SiPM working range, it has to be able to deliver light intensities ranging from single photons up to the saturation of the pixilated photodetector.

The thesis is structured as follows:
A short description of the LDC detector concept is given in Chapter 2, with particular emphasis on the hadronic calorimeter.
Chapter 3 serves as an introduction into the physics in a calorimeter, i.e. the interaction of particles with matter and hadronic shower development.
It is followed by Chapter 4, describing the calorimeter prototype with which the data in this thesis were taken.
In Chapter 5 the calibration and monitoring system of this physics prototype are introduced, with special emphasis on the light distribution system. The working principle of silicon photomultipliers is presented with focus on those characteristics requiring the calibration and monitoring system.
Chapter 6 contains the results of the data analysis. The non-linear SiPM response function is examined in a well controlled environment for a small sample of SiPMs, as well as for a much larger sample of SiPMs in the physics prototype with the calibration and monitoring system.
Conclusions and an outlook are given in Chapter 7.

Chapter 2

Large Detector Concept

Within the particle physics community it is widely agreed that the next collider will be a linear e^+e^- collider (ILC). The high luminosity at the ILC ($3.4 \cdot 10^{34}$ $cm^{-2}s^{-1}$) will allow very high statistical precision. Thanks to the clean environment in a lepton collider, the background and radiation damage in the detector are expected to be relatively low. Thus, the detector design is mainly driven by physics requirements. It has to be optimised for particle flow (PFLOW) concept, which promise a twice as good energy resolution as running experiments achieve [15]. The main goal of PFLOW concepts is particle separation. The physics program at the ILC sets some requirements on

- track momentum resolution:
  The precise determination of the Higgs boson mass from the leptonic decay of Z bosons $e^+e^- \rightarrow ZH \rightarrow l\bar{l}X$ is limited by the track momentum resolution.

- jet flavour tagging:
  Higgs boson to standard model fermion couplings are predicted to be proportional to the fermion masses. Therefore, a separation of b, c, and uds flavoured tracks is crucial. This can only be managed with a high precision vertex detector, as the heavy quarks do not live long enough to reach the other detector components.

- energy reconstruction:
  If no elementary Higgs exists the structure of the mechanism that provides electroweak symmetry breaking can be accessed analysing WW scattering. To do this analysis requires to distinguish between decays into Z pair and W pair final states respectively. Both modes decay dominantly into hadrons, and are therefore the quality of the reconstruction depends on the jet separation in the calorimeter. This postulates an unprecedented jet energy resolution.

- hermeticity:
  Missing energy in an event is a signature for many new physics channels, e.g.

supersymmetric particles. To distinguish these events from events in which the energy leaves undetected in form of particles close to the beam pipe, requires to detect down to as small polar angles as possible, and minimise dead material and cracks in the detector.

The *Large Detector Concept* assumes that the new challenges can be met best with a large volume Time Projection Chamber (TPC) as central tracker followed by highly granular calorimeters inside a coil that produces a 4 T magnetic field. Figure 2.1 shows the detector layout and dimensions.

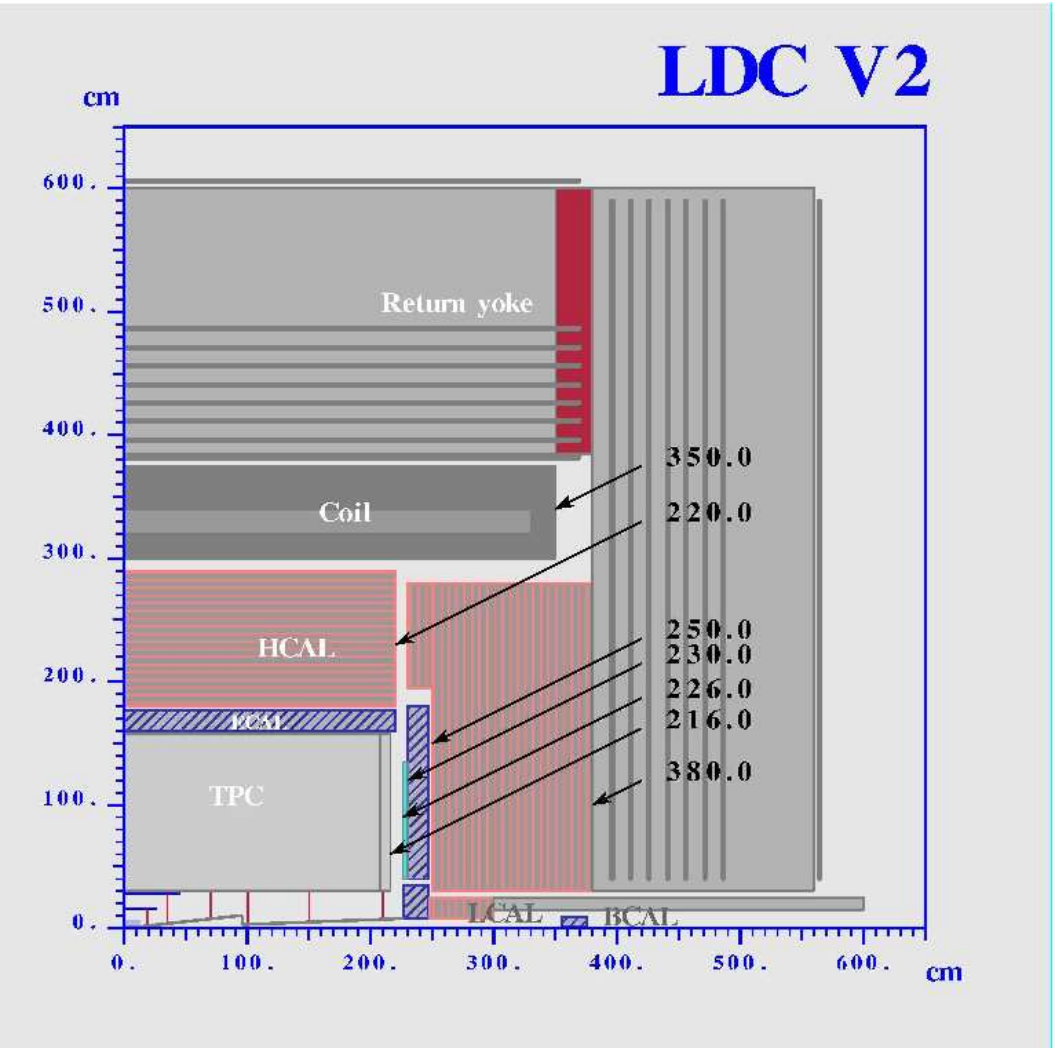

Figure 2.1: Sketch of one quadrant of the proposed LDC detector [7].

The vertex detector and silicon intermediate tracker are both pixilated silicon devices. Next comes a large volume time projection chamber (TPC) as main tracking de-

vice. The energy is measured in the electromagnetic (ECAL) and hadronic calorimeter (HCAL). All these detectors are operating in a 4 T solenoidal field and are surrounded by the instrumented flux return yoke, which also serves as muon detection system. The different parts of the LDC will be described in more detail in the following sections.

2.1 Particle Flow Algorithm

In average (but with a large spread due to fluctuations) 65% of the jet energy is coming from charged particles, 26% from photons and 9% from neutral hadrons. The different components of a detector are optimised to measure different types of particles: charged particles are best explored in tracking devices, the electromagnetic calorimeter (ECAL) is optimal to characterise photons, and neutral hadrons can be measured only in the hadronic calorimeter (HCAL). The particle flow (PFLOW) concept always uses the information from the component best suited for a given type of particle. The momentum of charged particles is very precisely measured in the tracking devices, and the calorimeters are left with the determination of neutral particles energy. This strategy implies the possibility to disentangle showers originating from charged and neutral particles.

The jet energy resolution can be described as:

$$\sigma^2_{\text{jet}} = \sigma^2_{\text{h}^\pm} + \sigma^2_{\gamma} + \sigma^2_{\text{h}^0} + \sigma^2_{\text{confusion}} + \sigma^2_{\text{threshold}} + \sigma^2_{\text{losses}} \tag{2.1}$$

In a perfect detector one would be able to reconstruct the tracks and energies of every single particle, as well as to perfectly separate charged and neutral particles. For this perfect detector the jet energy resolution is only limited by the energy resolution originating from charged particles $\sigma^2_{\text{h}^\pm}$, photons σ^2_{γ} and neutral hadrons $\sigma^2_{\text{h}^0}$. For a real detector there are also influences from the mixing between energy deposited by neutral hadrons and the debris charged hadrons interacting in the calorimeter $\sigma^2_{\text{confusion}}$, losses of particles due to imperfect reconstruction σ^2_{losses}, and the threshold energy $\sigma^2_{\text{threshold}}$ for each type of particles, below which an event is rejected.

In a perfect detector one can reach a jet energy resolution of $\sigma_E/E = 14\%/\sqrt{E}$ in Monte Carlo simulations [15]. Realistic simulations of an ILC detector indicate that a jet energy resolution of $\sigma_E/E = 30\%/\sqrt{E}$ at a centre of mass energy of $\sqrt{s} = 91$ GeV can be reached. This means that the jet energy resolution worsens by a factor two due to the confusion, losses and threshold terms. Studies on different thresholds in simulations resulted in modest effects. Hence, the optimisation of the detector should minimise the contributions from confusion and losses.

The minimisation of the confusion term can be achieved by the best possible association of deposited energy with the corresponding particle source. In addition, a three dimensional reconstruction of the shower is required. This allows a good pattern recognition and therefore a good shower separation (see Figure 2.2).

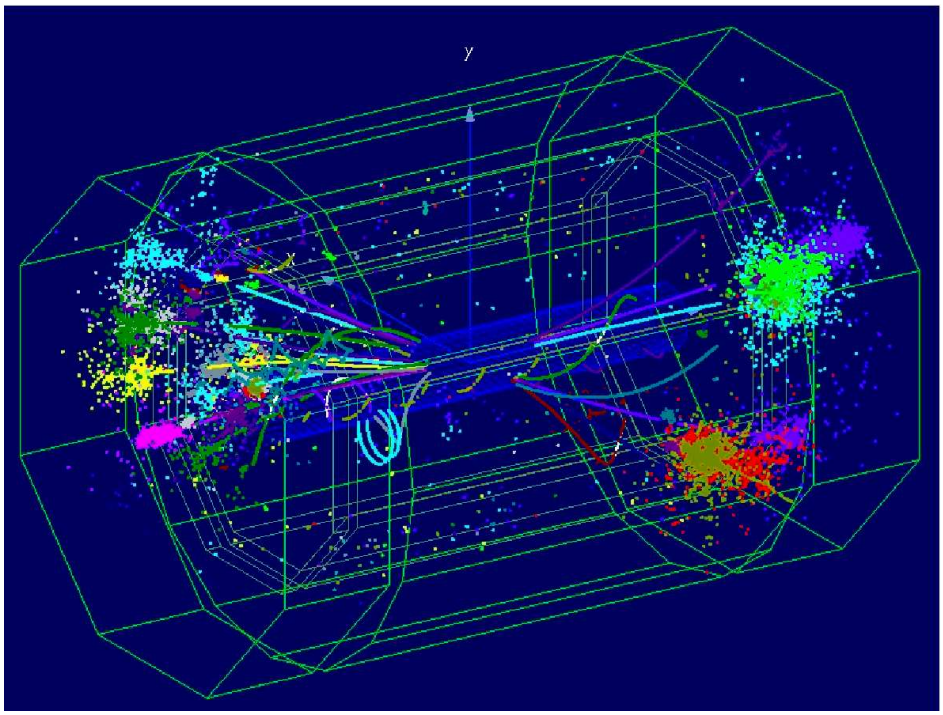

Figure 2.2: Three dimensional event display of a W boson pair decaying to jets at $\sqrt{s} = 500$ GeV in the LDC detector, obtained from a full detector simulation.

How to achieve a good separation of charged and neutral particles is illustrated for the ECAL separability

$$S_{\mathrm{h}^{\pm}/\gamma} \sim BL^2/\sqrt{\rho_{\mathrm{M}}^2 + \lambda_{\mathrm{int}}^2 + D_{\mathrm{p}}^2}\ . \tag{2.2}$$

The larger the separability, the better is the separation between charged particles and photons. Thus, charged particles and photons are better separated for high magnetic fields (B) and big inner ECAL radius (L). The separation is also improving with small Molière radius (ρ_{M} see Section 3.1), small hadronic interaction length (λ_{int} see Section 3.1) and small pad size (D_{P}). More detailed information about particle flow algorithms are given in [15].

2.2 Tracking and Vertex Detector

The tracking detectors are closest to the interaction point. They are used for precise track identification and momentum determination from the curvature of the reconstructed particle tracks.

The ILC physics program requires an excellent momentum resolution $\Delta(1/p) = 5 \cdot 10^{-5}$ (GeV/c)$^{-1}$ demanding a point resolution better than 150 μm [14]. An outstanding angular resolution in the forward region and a very good pattern recognition capability are needed as well. These aims can be fulfilled by a large volume time projection chamber in cooperation with a multi-layered pixel micro vertex detector followed by an additional silicon intermediate tracking detector and a precise forward chamber.

Many properties of an event can be reconstructed from the flavour of the final states. The produced heavy quarks decay almost immediately. Their secondary vertices can be determined very precisely in the vertex detector, this allows to reconstruct the primary particle. Therefore, this innermost part of the detector, with pixel size of the order of 20×20 μm^2 has to be precise enough to separate b and c quarks in the reconstruction.

A big TPC provides good 3 dimensional spatial and momentum resolution and information about energy losses ($\langle$dE/dx$\rangle$ see Section 3.2) through ionisation, while presenting a minimum amount of material in front of the calorimeters in the barrel region. New technologies for the read-out system for the TPC such as Gas Electron Multipliers (GEMs) [16] and Micromegas [17] are under development.

The gap between TPC and Vertex Detector is bridged by an intermediate silicon detector. This considerably improves the momentum resolution at large momenta, as it delivers a very precise track space point directly before the TPC. To improve the momentum resolution in the forward region, a precise forward chamber located behind the TPC end plates completes the tracking system. It enhances the tracking resolution at low scattering angles.

2.3 Calorimeter

Many new physics signatures will show up in complex hadronic final states. Hence, a key issue will be the reconstruction of jet four-momenta with high resolution. The biggest challenge is the separation of single showers originating from the same jet, as it is demanded for PFLOW concepts. Thus, excellent energy resolution, but also the capability to reconstruct photons coming from secondary vertices are necessary. If the detector can not tag (time-stamp) single bunch-crossings, hadronic two-photon events are accumulated over more than one bunch crossing. A good time resolution is needed to avoid this event pile-up. A highly granular calorimetric system will help to improve the knowledge of the longitudinal and transversal shower shape.

From experiments at the *Large Electron and Positron Collider* (LEP) and the *Stanford Linear Collider* (SLC) it is known that the best energy resolution for jets is reached using energy flow algorithms, similar to PFLOW algorithms. The success of this approach mainly depends on high lateral and transversal position resolution.

To get a good three dimensional picture of the shower development inside the calorimeter, the amount of inactive material in front of the calorimeter has to be minimised.

Therefore, the electromagnetic and the hadronic calorimeter are placed inside the magnetic coil. Hence, the calorimeters have to be compact, and a sandwich structure with a dense absorber material (high Z) is chosen for both. In addition, the high density results in a minimisation of the shower spread and thus leads to a good shower separation. Due to the high granularity of read-out cells, these "tracking"calorimeters are not only capable of measuring the overall energy of a shower, but to associate each shower with the originating particle.

The calorimetric system is completed by a beam calorimeter (BCAL), and a luminosity calorimeter (LCAL). Both of these low angle calorimeters serve as fast beam quality monitor and measure the luminosity. This improvement of hermeticity down to 5 mrad enhances missing energy resolution and provides the possibility to measure single bunch luminosity.

Electromagnetic Calorimeter

The high granularity requirements imposed on the electromagnetic calorimeter imply the necessity to read-out single cells with sizes close to the Molière radius of the absorber material employed. One option is a silicon-tungsten sandwich calorimeter. Tungsten allows a compact structure with 1×1 cm^2 pad size, which requires 32 million channels in total. The signal is read-out via silicon wafers.

An ECAL prototype with 40 readout layers is currently being built by the *CAlorimeter for the LInear Collider Experiment* (CALICE) collaboration. The first 13 layers of this ECAL prototype were tested in the DESY testbeam in January and February 2005. A more detailed description of this prototype is given in [11]. The ongoing development can be followed at [12].

Hadronic Calorimeter

There are at least two options for the read-out of a hadronic calorimeter (HCAL): an analogue scintillator steel calorimeter or a completely digital version. Both use stainless steel as absorber, which is less compact than tungsten but cheaper. A barrel module containing 38 layers, interleaved with 2 cm steel absorber plates, will cover 4.5 hadronic interaction lengths λ_{int}. An end-cap module of 53 layers will be 6.2 λ_{int} deep.

The digital hadronic calorimeter with wire chamber or resistive plate chamber read-out has a cell size similar to the ECAL. Due to cost reasons the high segmentation has to be compensated by giving up the information of the deposited energy per cell, resulting in a yes/no measurement only. As the number of cells hit is proportional to the energy, this can be compensated. This new technology has the benefit of an enormous transversal resolution, but it demands a huge amount of channels. More information about the digital calorimeter is given in [18].

A more classical solution is an analogue HCAL with coarser granularity than the digital version. A transverse cell size of 3×3 cm^2 was shown to provide very good shower separation [19]. The scintillation light can be read-out with a novel pixel photodetector device. The active area of these silicon photomultipliers (SiPM) is only 1×1 mm^2 and it is capable of working in strong magnetic fields. Therefore, it can be mounted directly on each tile. The energy deposited in each scintillator is proportional to the charge signal of the SiPM. A 1 m^3 physics prototype currently being built at DESY is described in more detail in chapter 4. The ongoing R&D can be followed at [20].

2.4 Magnet and Muon Chamber

A homogenous solenoidal magnetic field produced by a superconducting magnet will surround the tracking and calorimetric system. The magnetic field allows a high momentum resolution and separates the particles in a jet, both essential for particle flow reconstruction. Simulation studies about the impact of the magnetic field (2, 4, and 6 T) on PFLOW concept are ongoing [21].

The iron flux return yoke can be instrumented and serve as absorber for the muon detection system.

As the muon chambers have to cover a large area and will be hard to reach in need of exchanging detector elements later on, they have to be reliable and inexpensive. Resistive plate chambers were chosen for the LDC.

The occupancy in the muon system is expected to be low. At a centre of mass energy $\sqrt{s} = 500$ GeV only 5% of the charged particles reach the muon chambers. In order to study how much energy is leaving the HCAL, a prototype Tail-Catcher/Muon-Tracker consisting of scintillator strips and steel as an absorber, is being build at the moment. It will be placed behind the ECAL and the analogue HCAL prototypes in a combined testbeam run in summer 2006. Details on the Tail-Catcher prototype and results about a first combined testbeam run of one HCAL and one Tail-Catcher module will be given in [22].

Chapter 3

Physics in a Calorimeter

In high energy physics experiments at colliders high energetic particles are collided with each other. This leads to the production of new particles and possibly to new, undiscovered physics. These new particles interact with the detector material. The hadrons, on which this thesis focuses, reach the hadronic calorimeter, interact with it, losing part of their energy. The interaction process, mostly a result of strong or electromagnetic forces, depends on the energy and the nature of the particle, as well as on the material they traverse. In this chapter, various processes by which particles lose their energy and the showers that develop from these interactions are described.

3.1 Hadronic Showers

Due to the strong interaction in hadronic showers the variety of processes that may occur is large, and thus hadronic showers are complicated. Unlike in electromagnetic showers, where all energy is used to ionise the absorber and therefore can be measured, a certain fraction of the energy deposition of a hadronic shower is undetectable.

Charged hadrons ionise the materials' atoms, until at a certain depth, they strike a nucleus with which they interact strongly and can completely change their identity, e.g. turn into a few new hadrons. The struck nucleus may also change, lose some protons and neutrons and end up in an excited state from which it returns to ground state by emission of photons. Neutral hadrons can only interact strongly. The particles produced in the first reaction (mesons, nucleons, photons) may then lose energy through ionisation of the medium and/or by inducing new reactions. Mostly due to the photons from pion decays, a certain amount of a hadronic shower is electromagnetic.

The scales of a hadronic shower are different from pure electromagnetic ones. As the shower development is mainly based on strong interactions, it is described by the nuclear interaction length λ_{int}. The interaction length of a medium is defined as the average distance a high energetic hadron travels in this medium before interacting strongly.

It is bigger than the radiation length X_0, the typical scale on which electromagnetic showers evolve, e.g. $\lambda_{\text{int}}/X_0 = 9.5$ for iron. In high energy physics experiments hadrons traverse the tracking system and the electromagnetic calorimeter, with $0.9\lambda_{\text{int}}$ for the LDC, before interacting strongly mainly in the hadronic calorimeter, which is around $4.5 - 6.2\lambda_{\text{int}}$ deep in the LDC concept. The longitudinal profile of a hadronic shower is similar to that of a electron/photon induced shower. The number of particles in a developing shower rises roughly linearly, reaches a maximum and than decays again less steep than the rise. But despite this similarity hadronic showers are deeper and broader than electromagnetic ones, and the large fluctuations in their inner structure makes it more difficult to find an adequate parametrisation to describe them.

3.2 Electromagnetic Fraction in Hadronic Showers

Every hadronic shower contains an electromagnetic fraction, which mainly results from the decay of neutral pions into two photons. Charged particles ionise the medium they pass if their energy is sufficient to release atomic electrons from the Coulomb fields generated by the atomic nuclei. Electromagnetic interactions of charged particles are:

- excitation of atoms or molecules
  The excited states are unstable and usually quickly return to their ground state. In this process they emit one or more photons. If the energy differences are such that the emitted photons are in the visible range, this process is called scintillation and can be used to detect particles.

- emission of Cerenkov light
  If a charged particle travels faster than the speed of light in the medium, $v_{\text{particle}} > c/n$ where n is the medium's index of refraction, it loses energy by emitting photons at a characteristic angle. This mechanism is sensitive to the velocity of the particle and can be used to determine the mass of particles with known momenta.

- production of energetic knock-on electrons (δ-rays) at high energies
  In a high energetic collision between the passing particle and an atomic electron the electron can be knocked out of the atom.

- radiation of bremsstrahlung
  This is the most probable process at energies above 100 MeV. $e^{\pm}$ radiate photons as a result of Coulomb interactions with electric fields of atomic nuclei. For heavier particles with mass m ionisation remains the main contribution to energy losses up to higher energies. The critical energy E_c at which energy losses from radiation equal energy losses from ionisation is higher by a factor of $(m/m_e)^2$, where m_e is the electron mass, and thus 4000 times larger for muons, the next heavier leptons.

- induction of nuclear reactions at very high energies

The other main component in an electromagnetic shower are photons. They give rise to the following effects:

- Photoelectric effect
  At low energies this is the dominating process. An atom absorbs the photon and returns from an intermediate excited state to its ground state by the emission of an Auger electron.

- Rayleigh scattering
  The photon is deflected by the atomic electrons. However, it does not lose energy in this process and therefore this scattering only affects the spatial distribution and not the energy deposition.

- Compton scattering
  In this process the incoming photon is scattered by an atomic electron. The transfered energy and momentum to the struck electron is enough to put it in an unbound state.

- Pair production
  Photons with energies higher than twice the electron rest mass may, in the field of an atomic nuclei, create electron positron pairs. These pairs produce bremsstrahlung and ionisation along their way.

- Photonuclear reactions
  At energies ranging between 5-20 MeV photonuclear reactions, such as photo induced nuclear fission play a modest role. They have a maximum when the photon energy is approximately equal to the marginal binding energy of the proton or neutron. That is the difference in nuclear binding energies of the target nucleus and the target nucleus with one nucleon less.

A characteristic of high energetic electromagnetic shower, as shown in Figure 3.1, is particle multiplicity. The initial particle radiates photons on its way through the detector. Most of these have low energy and are absorbed through Compton scattering and photoelectric effect. Those with higher energies create e^+e^- pairs. Fast electrons and positrons can themselves radiate more photons, which results in an electromagnetic cascade. The shower energy is deposited in the absorber through ionisation by the electrons and positrons. As the number of these particles increases while the shower is developing, the energy deposition also increases with growing shower depth. However, the average energy of the shower particles decreases, and after a certain maximum the energy is too low to produce further e^+e^- pairs and the shower dies out.

The electromagnetic shower is characterised by the radiation length X_0 and the Molière radius ρ_M in longitudinal and lateral direction respectively. One radiation length corresponds to the distance after which electrons and positrons lose on average $1 - 1/e = 63.2\%$

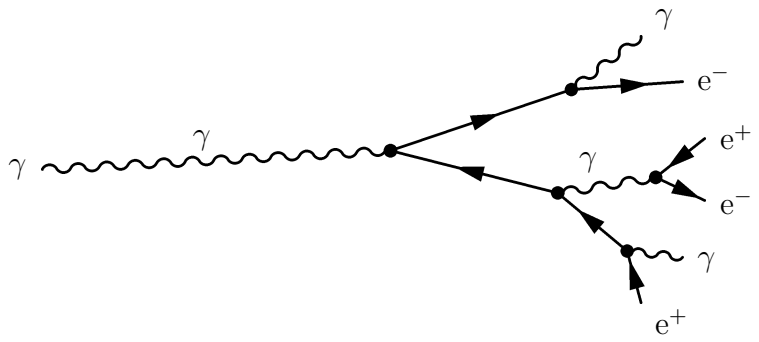

Figure 3.1: Feynman diagram of a simple electromagnetic shower induced by a photon.

of their energy due to bremsstrahlung. The Molière radius ρ_{M} is defined in terms of the radiation length: $\rho_{\mathrm{M}} = E_{\mathrm{s}}\frac{X_0}{E_{\mathrm{c}}}$. Where E_{c} is the critical energy, and E_{s} is the scale energy $E_{\mathrm{s}} \approx m_{\mathrm{e}}c^2\sqrt{4\pi/\alpha} = 21.2$ MeV. On average 90% of the shower energy is deposited in a cylinder with radius ρ_{M} around the shower axis.

Ionisation Energy Loss by Heavy Particles

Charged particles other than electrons, e.g. muons, lose their energy primarily through ionisation. The mean energy loss per unit path length $-\langle \mathrm{dE/dx} \rangle$ is given by the Bethe-Bloch-formula:

$$-\langle \mathrm{dE/dx} \rangle = \mathrm{Kz^2}\frac{\mathrm{Z}}{\mathrm{A}}\frac{1}{\beta^2}\left[\frac{1}{2}\ln\frac{2\mathrm{m_e c^2}\beta^2\gamma^2\mathrm{T_{max}}}{\mathrm{I^2}} - \beta^2 - \frac{\delta}{2}\right] , \tag{3.1}$$

in which T_{max} equals the maximum kinetic energy that can be transferred to an electron in a single collision, I is the mean excitation energy of the absorber material and δ is a correction term describing the density effect. The proportionality constant K is $4\pi N_{\mathrm{A}} r_{\mathrm{e}}^2 m_{\mathrm{e}} c^2$, where N_{A} is Avogadro's number and r_{e} is the classical electron radius.

As shown in Figure 3.2, the energy loss by ionisation decreases until a minimum around $\beta\gamma = 3 - 4$. After this minimum ionisation value, the energy loss rises again. For particles with energies $E > E_{\mathrm{c}}$ energy losses by radiation of bremsstrahlung dominate. Charged particles with energies below E_{c}, but higher than $\beta\gamma = 1$ are called minimum ionising particles (MIPs). They lose very little energy on their way through a medium.

3.3 Calorimeter Response

A calorimeter can either be build homogeneously, i.e. the entire volume is sensitive to particles and can contribute to the signal, or as a sampling device, consisting of a

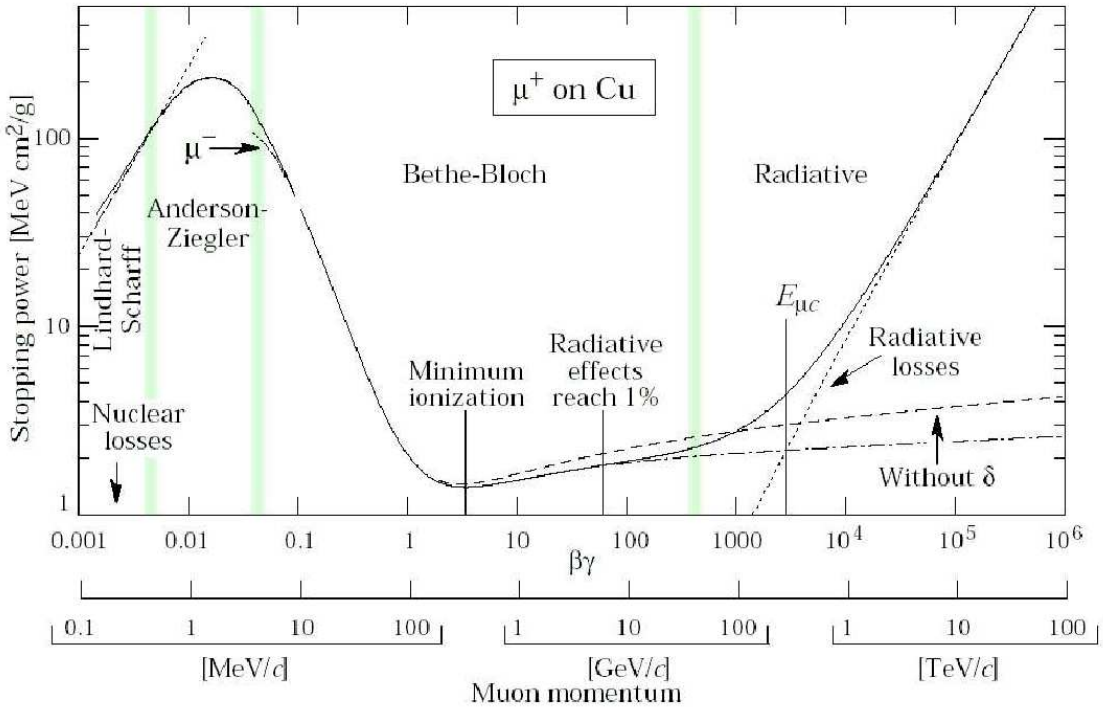

Figure 3.2: Stopping power for muons in copper [24].

passive high density absorber interleaved with active material that generates the signal. Separating nearby jets, as required for the particle flow concept, demands a fine lateral granularity of the active material. In addition a good longitudinal resolution and thus thin absorber layers allow to extract the shower profile, which is needed to identify the particle that induced it. The high longitudinal granularity can only be achieved for sampling calorimeters. Another important characteristic of a calorimeter is the shower containment, i.e. the fraction of the shower that is inside the calorimeter. The choice of a high-Z absorber material results in more compact dimensions for a sampling calorimeter than for a homogenous one with the same shower containment.

The energy resolution of a calorimeter is an important performance characteristic. It limits the precision with which the mass of a particle can be determined and the separation between particles with similar masses. Statistical fluctuations in the energy deposition and the technique chosen to detect the final products of the particle cascade limit the energy resolution. The statistical fluctuations obey the rules of Poisson statistics, changing with $\sqrt{E}$, i.e. the relative energy resolution $\frac{\sigma_E}{E} \propto \sqrt{E}/E$ improves with increasing energy. The main technical limit is electronic noise. The contribution from

noise fluctuations scales like $\propto E^{-1}$. This component dominates at low energies. A third component is due to errors in the calibration of the chosen detector read-out technique, e.g. gain instabilities in photomultiplier tubes. This term is energy independent. The different terms are uncorrelated, thus the total energy resolution is:

$$\frac{\sigma_E}{E} = \frac{a}{\sqrt{E}} \oplus \frac{b}{E} \oplus c = \sqrt{\left(\frac{a}{\sqrt{E}}\right)^2 + \left(\frac{b}{E}\right)^2 + c^2}\ , \tag{3.2}$$

in which $a/\sqrt{E}$ is caused by the statistical fluctuations, b/E corresponds to the noise factor and c is the constant term due to calibration errors. Especially in the last term the calibration of the calorimeter channels, its inhomogeneity and stability play and important role. This thesis is exploiting the monitoring system to reduce the fluctuations due to temperature and voltage variations. These fluctuations effect the constant term c in Equation 3.2.

Chapter 4

Physics Prototype

An analogue hadronic sandwich calorimeter with high longitudinal and transverse granularity holds the promise of meeting the demands of spatial and energy resolution imposed by the particle flow concept for the ILC [25]. A 1 m^3 physics prototype with 2 cm steel absorber plates and scintillator tiles as active medium is currently being built at DESY in cooperation with other institutes from the CALICE collaboration (R&D see [11]). The physics prototype is meant to explore hadronic shower development with unprecedented granularity in order to validate hadronic shower simulation models and to develop energy weighting and particle flow reconstruction algorithms. The data needed to examine these topics will be taken in a combined testbeam run at the *Super Proton Synchrotron* (SPS) at CERN together with the ECAL and Tail-Catcher prototypes in summer 2006. The testbeam delivers different particles (pions, protons and muons) within an energy range of 15 to 100 GeV. Furthermore, the incident angle of the particles can be varied by changing the detector position with a movable table.

The basic tile size of $3 \times 3 \times 0.5$ cm^3 is optimised with respect to particle separation capabilities. In order to reduce costs the high granularity is restricted to the first 30 layers, with 100 3×3 cm^2 tiles in the core. This core is surrounded by larger (6×6 and 12×12 cm^2) tiles, resulting in 216 channels for each of the first 30 layers and 141 channels for the last 8 layers, which miss the high granular core. Figure 4.1 is a schematic top view of both layer configurations. Overall around 8000 channels have to be calibrated, monitored and read-out for the entire physics prototype.

The read-out of this amount of scintillator tiles will be realised with silicon photomultipliers. Due to its small size of 1×1 mm^2 this new photodetector can be mounted directly on each tile. This has the advantage, that the light is converted into an electronic signal at an early stage. Thus, there is no need for a complicated light guidance system to transport the light out of the module towards a photodetector, and losses due to light transport and coupling are minimised. The scintillation light is collected by a wavelength shifting fibre inserted into a groove and guided to a SiPM (in the front right corner of Figure 4.2). Micro-coax cables with 1 mm diameter guide the SiPM

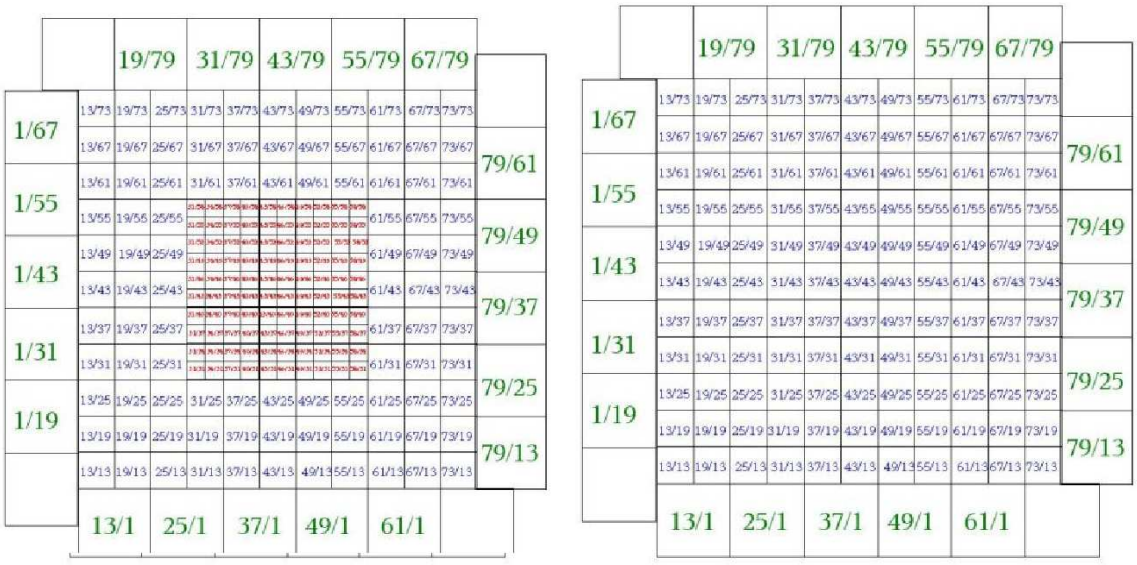

(a) (b)

Figure 4.1: Top view of the scintillator tile layout used for the physics prototype. (a) Layer 1-30 with high granular core. (b) Layer 31 - 38 with coarser segmentation.

signal to the read-out electronics. They are fixed on top of a plastic (FR4) board that covers all tiles. This board also serves as support for the calibration light fibres.

4.1 Read-out chain

A particle traversing the hadronic calorimeter produces light in a scintillator tile. Organic scintillating molecules in polystyrene (BASF 130) produced by the Vladimir company, emit scintillation light with a wavelength of about 430 nm (see Figure 4.3(a)). The edges of each tile are chemically treated to limit optical crosstalk to $< 2\%$ [26]. A wavelength shifting (WLS) fibre (Y11, 300 ppm) from Kuraray placed in a groove inside the tile is absorbing the ultraviolet (UV) scintillation light and re-emits green light with a peak wavelength around 500 nm (see Figure 4.3(b)). This enlarges the light detection efficiency, as the SiPMs are more sensitive to green, due to the quantum efficiency of silicon. Reflection foils (VN2000 superradiant from 3M) above and below the tiles and a mirror on one end of the WLS fibre minimise light losses. On the other end of the fibre, the collected light is detected by a silicon photomultiplier (see Chapter 4.2). The optical path of a signal is shown schematically in Figure 4.4.

The SiPM signal is amplified by a charge amplifier and shaped in an Application-

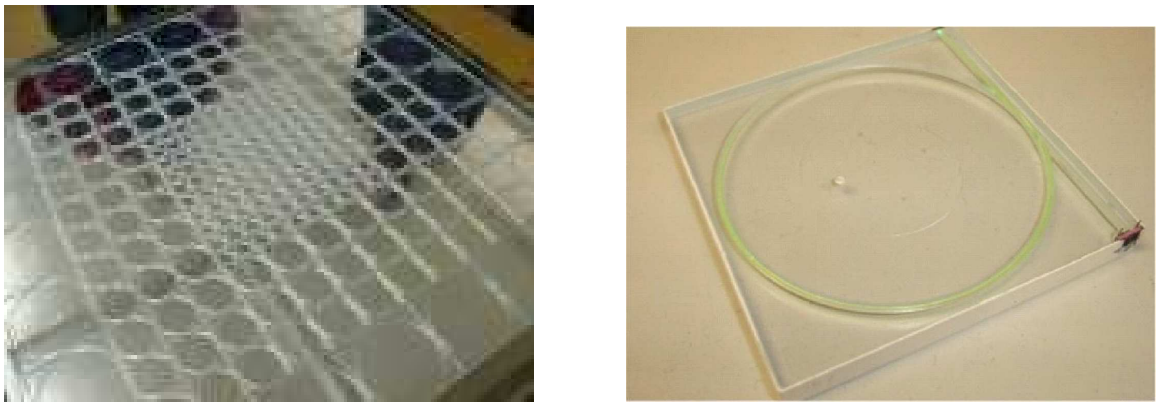

(a) (b)

Figure 4.2: (a) Picture of the first completed tile mosaic of the physics prototype. (b) Fully equipped scintillator tile with a WLS fibre guiding light to a SiPM in the front right corner.

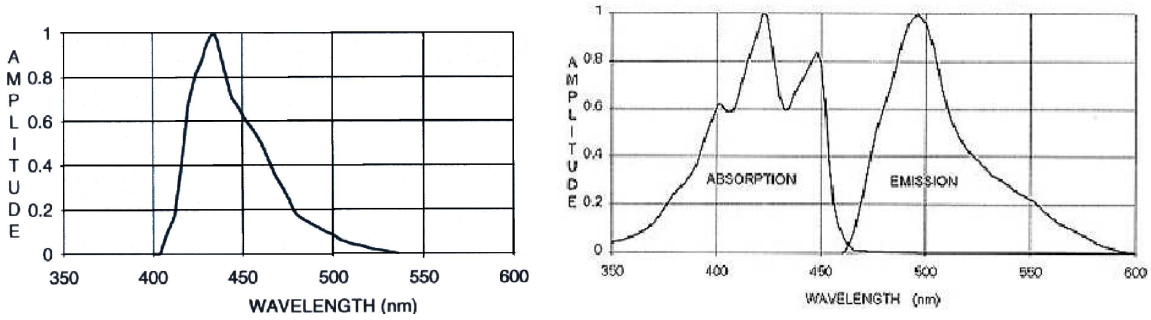

(a) (b)

Figure 4.3: (a) Emission spectrum of the used scintillator. (b) Absorption and emission spectrum of the WLS fibre.

Specific Integrated Circuit (ASIC) chip designed by *Laboratoire Accélérateur Linéaire* (LAL). A detailed description of this chip can be found in [27]. The ASIC chip is used in two different working modes, the so called calibration and physics mode, to optimally fit the complete SiPM working range with the used 16-bit analogue to digital converter (ADC) range. For small signals the shaping time is short (40 ns) and the amplification is high (approximately factor 100). In this calibration mode single photoelectron spectra can be observed. For higher signals less amplification is needed. The physics mode used for these signals has an amplification of approximately factor 10.

This has the advantage that the ADC range is not exceeded. Furthermore, the shaping time in physics mode is longer (200 ns). The longer shaping time provides the latency for the beam trigger. It has the disadvantage that it is not possible to observe single photo-electron spectra in this mode, as it also integrates over the SiPM dark rate. The PIN photodiode is operated in its own mode with short shaping time (40 ns) and medium amplification (approximately factor 40).

One chip reads the signal from 18 SiPMs and transform them into one multiplexed output signal that is then passed through the CALICE readout card (CRC), containing 16-bit analogue to digital converters. The CRC has 8 input ports, each receiving the signal from 12 ASIC chips. This results in 5 CRC boards inserted into one 9 unit VersaModule Eurocard (VME) crate to read-out the whole physics prototype. The CRC signal is proceeded through the VME bus and a VME-PCI interface to the data acquisition. The signal path is illustrated in Figure 4.5.

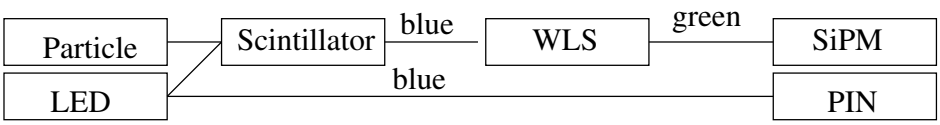

Figure 4.4: Abstract illustration of the optical path of a signal from the particle or the LED light induced scintillation light to the photodetector.

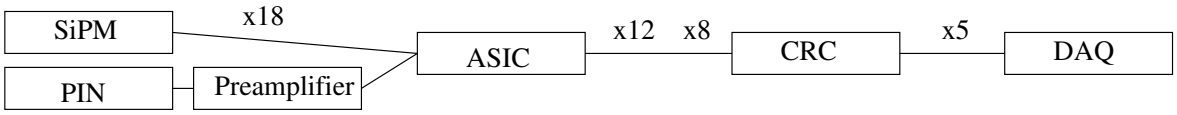

Figure 4.5: Abstract illustration of the logical path of a signal from the photodetector to the data acquisition.

4.2 Silicon Photomultiplier

A silicon photomultiplier produced by the *Moscow Physics and Engineering Institute* (MEPhI) and *Pulsar enterprise*, as it is shown in Figure 4.6(a), is a semiconductor based photodiode with high gain and low noise. This multi-pixel analogue device consists of about 1000 pixels joint on one common silicon substrate with ~ 1 mm^2 area. Each pixel operates as an individual photon counter. They are operated in limited Geiger

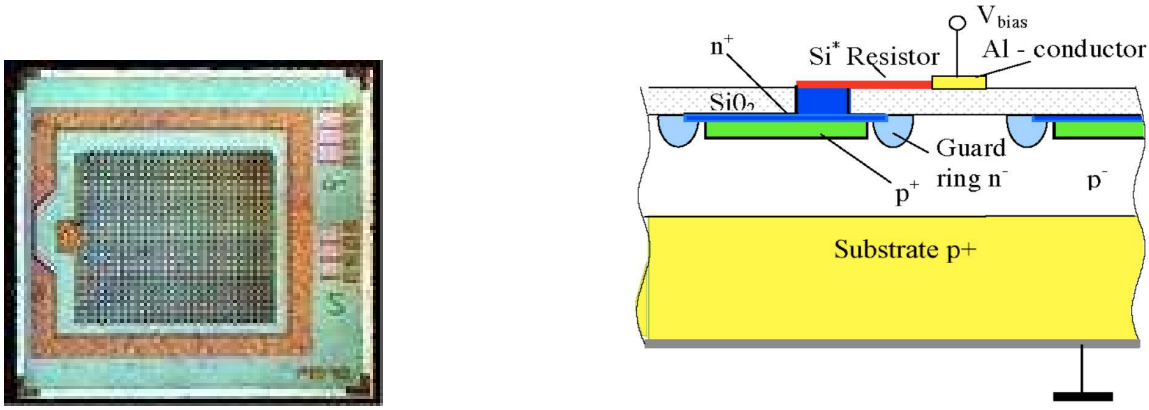

(a) (b)

Figure 4.6: (a) Picture of a silicon photomultiplier mounted on a support plate. (b) Scheme of one SiPM pixel [28].

mode at $10 - 20\%$ over breakdown voltage. Each carrier, created by signal or thermal noise, gives rise to a Geiger discharge. Therefore, the single pixel signal is independent of the amount of incident carriers. Anyhow, the amount of fired pixels depends on the amount of incoming photons, thus the overall signal, the sum of all fired pixels, is an analogue one.

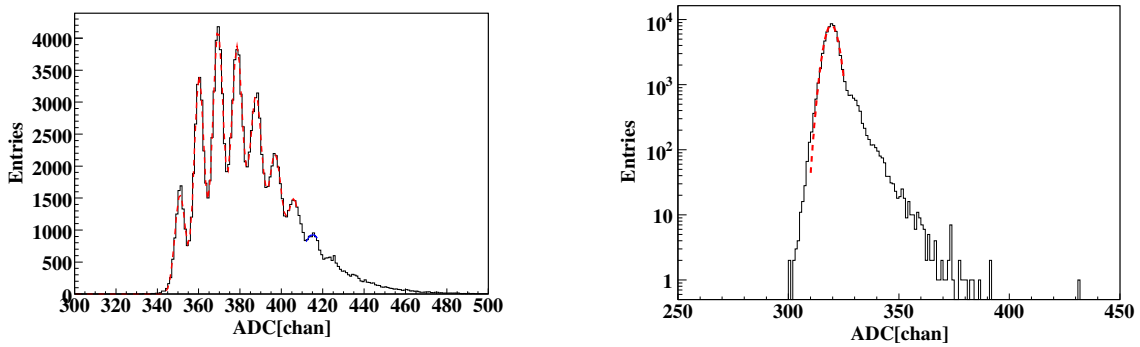

(a) (b)

Figure 4.7: (a) Single photo-electron spectrum displayed by a SiPM illuminated with low intensity LED light (b) SiPM pedestal in logarithmic scale.

Gain is defined as the number of secondary electrons generated in the discharge cascade

produced by a primary photo-electron, an electron induced by an incoming photon through the photo-effect. The charge Q_{pix} collected in one SiPM pixel is typically a few 100 fC $\sim 10^6$ e [28]. Hence, the SiPM gain is in the same order of magnitude as the gain of vacuum photomultiplier tubes. For low light intensities, the SiPM displays a single photo-electron spectrum, as given in Figure 4.7(a). The zero peak is a pedestal peak, the first peak is the signal from one photo-electron firing one pixel, the second from two, and so on. The distance between two peaks equals the SiPM gain in ADC channels per pixel.

Figure 4.7(b) shows a pedestal spectrum from a SiPM in logarithmic scale. The long tail to the right is a convolution of two SiPM properties, namely dark rate and crosstalk. Due to thermal noise a pixel can fire spontaneously without any incident photon, this is the reason for the dark rate. A fired pixel can also optically fire neighbouring pixels due to the production of photons in the ionisation avalanche. As a result of this inter-pixel crosstalk more than one pixel can be fired by one photo-electron. These effects are mainly dominant at low light intensities, where the number of photons is much smaller than the total number of pixels.

For larger signals saturation effects, caused by the limited amount of pixels on a SiPM and the finite pixel recovery time τ, outbalance the crosstalk effect. A quenching resistor $R_{\text{quench}} \approx 2 - 20$ MΩ on each pixel stops the Geiger discharge. The time before a pixel can fire again $\tau = R_{\text{quench}} \cdot C_{\text{pix}}$ is determined by this resistor. The SiPM capacitance is typically $C_{\text{pix}} \approx 50$ fF [29], resulting in a recovery time $\tau \approx 100 - 1000$ ns. Due to this recovery time, not every photo-electron is firing a pixel at high light intensities. Both effects have to be corrected for to recover the real signal from the non linear SiPM response. The response function that is describing this property can be measured under very defined conditions with optical filters to control the amount of light. This method is explained in Section 6.2.1.

The photon detection efficiency (ϵ_{PDE}) for photomultiplier tubes is determined by the quantum efficiency (ϵ_{QE}), i.e. the probability for the incident photon to release the primary photo-electron. For SiPMs one has to take into account in addition geometrical efficiency $\epsilon_{\text{geo}} = A_{\text{pix}}/A_{\text{tot}}$, as only part of the SiPM total area (A_{tot}) is sensitive to light, and ϵ_{Geiger} the probability for a carrier to initiate a Geiger discharge. The SiPM photon detection efficiency is defined as:

$$\epsilon_{\text{PDE}} = \epsilon_{\text{QE}} \cdot \epsilon_{\text{geo}} \cdot \epsilon_{\text{Geiger}}$$

Gain (G_{pix}) and photon detection efficiency vary with temperature and bias voltage. Thus, the charge (Q) collected by the SiPM, which is a convolution of gain and photon detection efficiency, also varies with temperature and bias voltage [30]:

$\text{dG/dT} = -1.7\%/\text{K} \quad \text{dG/dV} = +2.5\%/0.1\ \text{V}$
$\text{dQ/dT} = -4.5\%/\text{K} \quad \text{dQ/dV} = +7\%/0.1\ \text{V}$

Due to these dependencies the SiPM signal has to be corrected for temperature and voltage changes, thus a monitoring system is necessary. This system can also be used

to monitor changes of the SiPM response function (with temperature, voltage, or due to dying pixels).

Chapter 5

Calibration and Monitoring System

As described in the last chapter, the signal from the photodetectors used to read-out the scintillator tiles in the calorimeter prototype is temperature and voltage dependent. This requires constant monitoring and correction, in order to get the correct signal height. The monitoring system designed for this physics prototype has the ambitious goal to monitor the whole optical chain, i.e. scintillator tile, wavelength shifting fibre and SiPM. This can be realised with a system of light emitting diodes (LEDs see Section 5.1.1) monitored by PIN photodiodes SFH250 from Hamamatsu (see Section 5.1.3). Each LED illuminates a bundle of 19 clear fibres out of which 18 guide the light to SiPMs. The centre fibre of such a bundle leads to a PIN photodiode, to monitor the LED light amplitude. This results in almost 500 LEDs and PIN photodiodes to monitor the total calorimeter prototype.

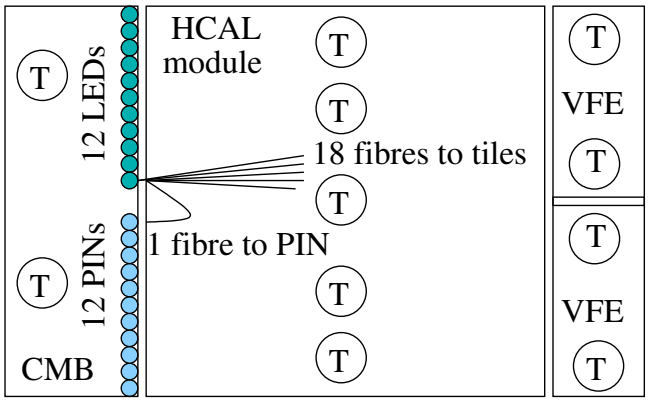

Figure 5.1: Schematic view of one physics prototype layer equipped with a calibration and monitoring board (CMB), temperature sensors (T) and very frontend electronics (VFE).

Figure 5.1 shows a schematic view of one HCAL physics prototype layer. The cali-

bration and monitoring board (CMB) on the left side is designed by the *Institute of Physics, Academy of Science of the Czech Republic* in Prague. Each CMB provides 12 LEDs. The light of each LED is distributed to 18 SiPMs and one PIN photodiode to monitor the LED signal. On this board the LED drivers, controlling the LED pulse height and width, as well as low noise PIN preamplifiers are located. To simplify the read-out system, the PIN photodiodes will be read-out by the same electronics used for the SiPMs. As the LED light is attenuated by the scintillator and the wavelength shifting fibre before it reaches the SiPMs, and directly passed to the PIN photodiodes, the light yield in the PIN photodiodes is roughly 200 times larger than that of the SiPMs. But as the SiPMs have an intrinsic gain of $\sim 10^6$ and the PIN photodiodes have a gain of 1, the PIN signal still has to be preamplified as soon as possible, to minimise signal losses, before it can be passed to the further electronic read-out chain.

The temperature is monitored by two temperature sensors on the CMB, five more on the module and four on the very frontend electronic (VFE) boards. They are part of a slow control system, that also monitors the voltages and currents of all SiPMs. This provides redundant information on the measurements of the calibration and monitoring system.

The very frontend electronic is placed opposite to the CMB to minimise electronic crosstalk. It contains an ASIC chip that is amplifying and shaping the signals from the SiPMs. The ASIC integrates for a defined time the incoming charge of the signals and shapes the preamplified signal with a bipolar shaper. The signals from 18 SiPMs are then held at their maximum amplitude and multiplexed, before they are passed on to the frontend electronics.

5.1 Light Distribution System

The light from each LED has to be distributed to 18 SiPMs and one PIN photodiode. A big effort was put into this distribution system to ensure equal light in all detectors connected to one LED. Single photo-electron spectra can only be observed at small, but not too small light intensities. Thus the light intensity should be as uniform as possible to match this small region that is used to determine the SiPM gain. After optimisation of the LED to bundle and the fibre to scintillator tile couplings, the finally used distribution system achieved less than a factor two between the brightest and the dimmest fibre output signal. Figure 5.2 proves that such single photo-electron spectra can be obtained for all SiPMs connected to one LED for one LED voltage setting.

5.1.1 Light Emitting Diodes

A light emitting diode is a p-n-junction made of compound semiconductors, e.g. gallium arsenide. A voltage across the junction in forward direction introduces a current flow.

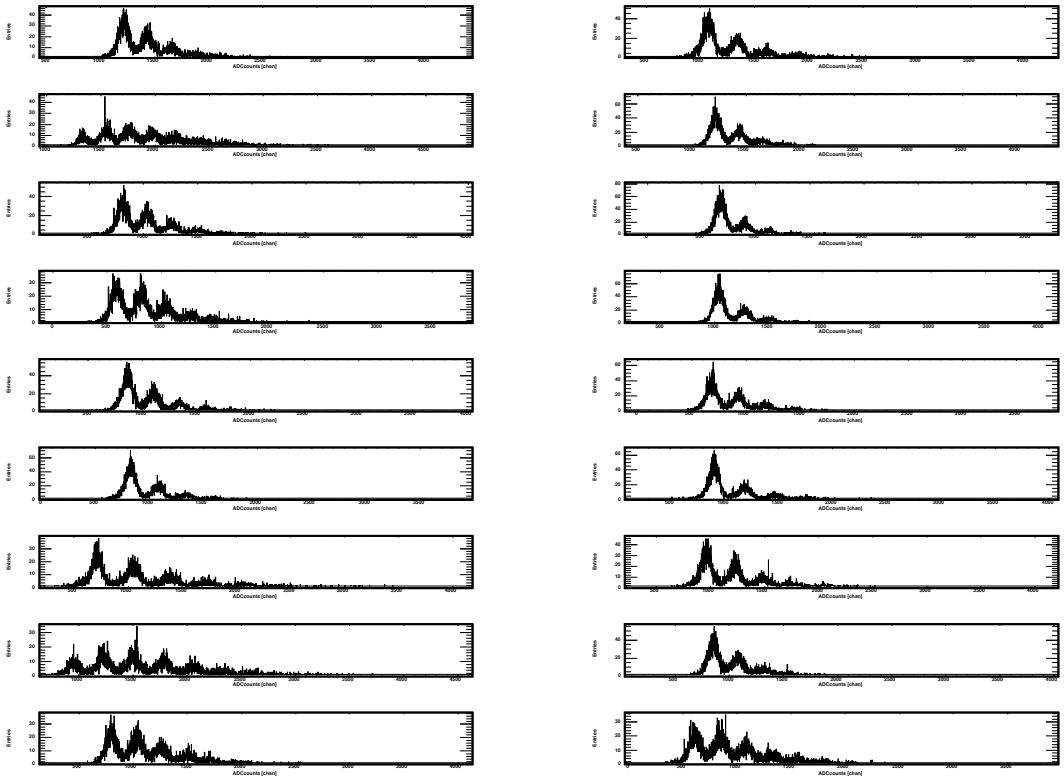

Figure 5.2: Single photo-electron spectra for all 18 SiPMs connected to one LED received for one LED voltage setting, plotted in number of entries versus ADC channels.

Holes from the p region and electrons from the n region recombine to allow the current flow. In this process a part of the energy is released as photons.

Light emitting diodes have a long life time, small size, and low supply voltage. In addition the calibration and monitoring system requires a homogenous light cone, as one LED illuminates 18 SiPMs. One more premise needed is enough light to saturate the SiPMs, which is needed to monitor changes in the number of active pixels on the SiPM. Therefore, the LED should be very bright. Both extremes should be covered with as less LED settings as possible to keep the time needed for calibration and monitoring short, in order to minimise the impact on physics data taking.

The light cone uniformity of the LEDs is tested by rotating the LEDs around 360° and detecting the light output with a wavelength shifting fibre connected to a PIN photodiode. In addition the radial variation is tested with the same setup for various LED light amplitudes. The spread between brightest and dimmest LED intensity is found to be less than 1.5 (see Figure 5.3).

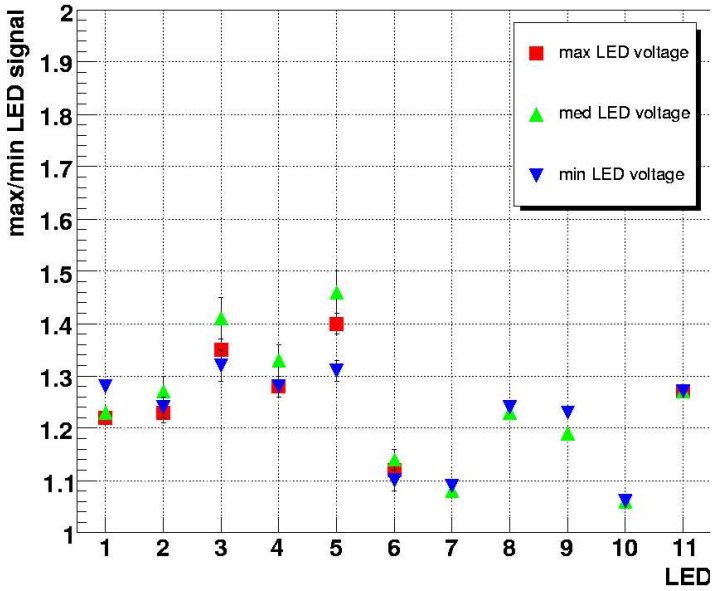

Figure 5.3: Light cone homogeneity test for 11 LEDs showing the ratio between maximum to minimum light intensity.

The LED signal is meant to imitate the signal of a particle passing the detector. Thus, it should be short (10 - 20 ns) with a fast rise and fall time. This is realised with a fast LED driver, developed specifically for the calibration and monitoring system by the Prague institute. At the beginning this driver is reverse biasing the LED. The polarity on the LED legs is switched for 10 - 20 ns, during which the LED is shining. The following switch back to reverse-bias ensures a very fast stop of the signal. Figure 5.4(a) shows an oscilloscope picture of the voltage applied to the LED legs. The resulting voltage on the LED is the difference of both curves, as shown in plot (b). Figure 5.5 shows the signals from a PIN photodiode (smaller red signal) and a SiPM (bigger black signal) after ASIC for a bright light pulse with two different settings of gain and shaping time in the ASIC chip, which are optimised to read-out the two photodetectors respectively.

The final driver, controlled by the data acquisition, is able to pulse 12 LEDs per CMB simultaneously and to control the pulse width and the LED amplitude. A prototype driver that is capable of operating two LEDs is used to take the data analysed in this thesis.

5.1.2 Light Distribution

One LED illuminates a bundle of 19 double-clad transparent fibres with 0.75 mm diameter. These fibres are glued together at one end. The most critical part of the

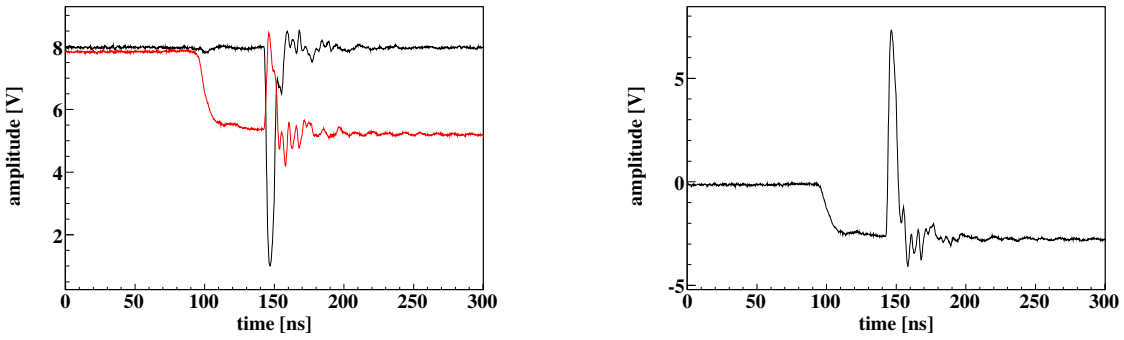

(a) (b)

Figure 5.4: Oscilloscope picture of the time development of (a) the different potentials applied to the LED legs, and (b) the resulting voltage impressed on the LED.

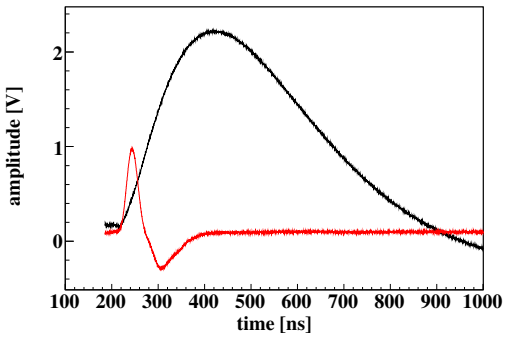

Figure 5.5: Signal from the PIN photodiode (short red) and the SiPM (long black) after amplification and shaping using the ASIC chip.

light guide system is the coupling between LED and bundle, and between fibre and PIN photodiode respectively. Special connectors were developed to ensure mechanical stability and to reduce the spread in the light distribution. The glued bundle end is polished and then fixed centric to the LED with a metal sleeve (see Figure 5.6). The loose ends of 18 fibres are inserted into aluminium alloy (AlCuMgPb) mirror caps. The caps reflect the light of the fibre to the scintillating tiles underneath. This ensures a mechanically stable and reproducible connection to each scintillator (see Figure 5.7(a)). The centre fibre of each bundle, which usually gets the most light from the LED, is connected to a PIN photodiode. A special connector (Figure 5.7(b)) provides a mechanical stable contact between fibre end and PIN photodiode.

(a) (b)

Figure 5.6: (a) A glued light guidance fibre bundle surrounded by a metal sleeve. (b) The same bundle fixed centric in a module by the metal sleeve.

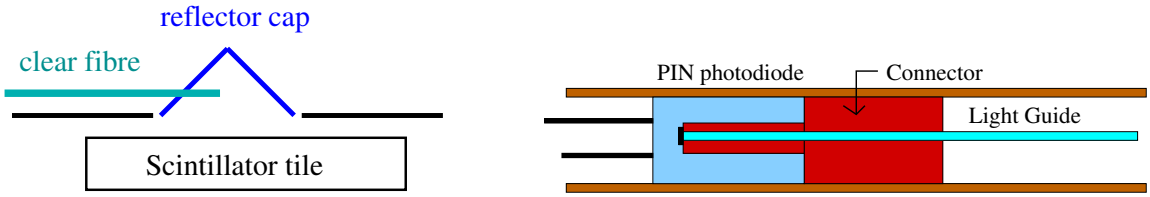

(a) (b)

Figure 5.7: (a) Schematic view of an aluminium alloy mirror on top of a scintillator tile with a light distributing fibre ending in the middle of the reflector. (b) A brass connector (red) centres the loose fibre end in front of the sensitive area of the PIN photodiode.

The light spread in this light distribution system is less than a factor 2. As proved in Figure 5.2, this matches the requirement to obtain single photo-electron spectra for all SiPMs supplied by one LED for one LED voltage setting. Unfortunately, all the efforts to optimise the amount of light in the SiPMs inevitably leads to relatively low light in the PIN photodiodes. As the dynamic range needed to monitor the full SiPM working range, just can be covered with the used calibration and monitoring system, the ranges in which the SiPM and the PIN photodiode work have to be adjusted very carefully. At the moment the SiPMs are responsive to less light than the PIN photodiodes. This still has to be solved, e.g. by attenuating the light in the SiPMs with a half transparent aperture, that covers the glued bundle end except a small hole for the centre fibre.

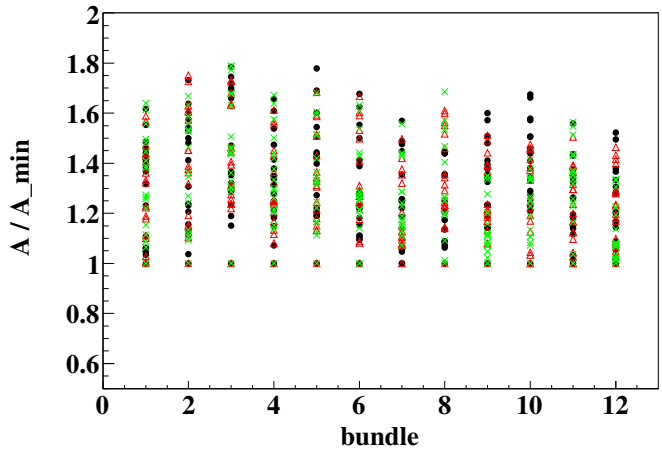

Figure 5.8: The spread in light intensity for different fibre bundles connected to one LED. Each bundle consists of 18 fibres. The light intensities of the fibres are normalised to the light intensity of the dimmest fibre in the bundle.

5.1.3 PIN Photodiodes

The monitoring system has to be monitored, to disentangle LED amplitude variations, as they might appear from temperature dependencies, ageing and fluctuations in pulse width and pulse height from changes of the SiPM signal. Therefore, a PIN photodiode is connected to the centre fibre of each bundle to monitor the LED light intensity, as described in the previous section.

A PIN photodiode is a p-i-n junction with an intrinsic layer between the p and the n region. It is operated under moderate reverse bias to keep the depletion region free from charge carriers. A photon entering the intrinsic layer may strike an atom, set an electron free, and thus create an electron-hole-pair. The electron and the hole migrate in opposite directions due to the applied electronic field across the diode. This introduces a small current flow proportional to the number of incident photons.

PIN photodiodes have no intrinsic gain. Hence, their signal does not depend on temperature fluctuations, and it can be used as a reference. The dynamic range shown in Figure 5.9(a) is limited by the signal over noise ratio of the preamplified PIN photodiode signal in the low light region. It rises linear with increasing LED current, until the saturating LED light intensity at high currents gives the upper limit of the dynamic range. Figure 5.9(b) shows the residual of the linear fit given in Figure 5.9(a), where the residual is $(y_{\text{point}} - y_{\text{fit}})/y_{\text{fit}}$.

In principle this dynamic range would be sufficient to monitor the LED light intensity over a range that is big enough to cover the full SiPM working range. But at the

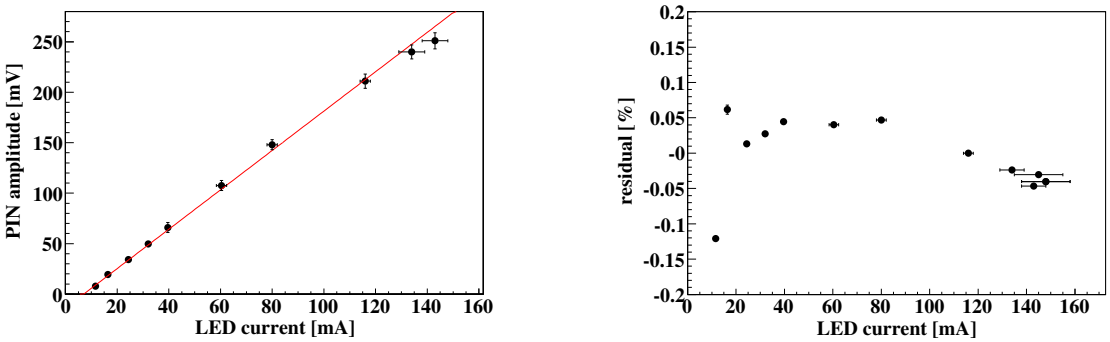

(a) (b)

Figure 5.9: (a) Voltage amplitude of the PIN photodiode after preamplifier versus the LED current. (b) Residual of the linear fit in plot (a).

moment these two working ranges, from the SiPMs and the PIN photodiodes, are not matched good enough. Thus, it is currently not possible to observe PIN photodiode signals in the light intensity range that covers the SiPM calibration mode. One solution to better adjust these ranges would be to give less light to the SiPMs, as described in the previous section. Perhaps it is also possible to monitor the SiPM behaviour at higher signals than at the few MIP level which currently is proposed. If this is the case, the PIN photodiode signal will be allowed to start at higher light intensities and will be correlated to the SiPM signal in physics mode. Investigations on this topic are ongoing.

Chapter 6

Response Function of the Silicon Photomultiplier

In order to extract the information of energy deposited in a calorimeter cell, the photodetector signal has to be calibrated. The charge signal from the photodetector does already contain the conversion of particle energy into scintillation light and of light into charge. The task of the calibration procedure is to go backwards in this chain, to get back the energy information out of the charge collected in the photodetector.

For a photodetector with linear response, e.g. a photomultiplier tube, only one constant number is required to fix the slope between ADC channels and corresponding energy. Typically this is done at the energy equivalent to one minimum ionising particle (MIP, see Section 3.2). SiPMs have a non-linear response due to the limited amount of pixels, the finite pixel recovery time and crosstalk effects. Therefore, one unique number is not sufficient to calibrate them. In addition to the ADC channels to energy calibration, one has to correct the measured ADC value for the SiPM response.

For a single channel it would be possible to calibrate the system with the response function expressed in ADC channels versus energy. When dealing with a multi-channel system like the HCAL, it is preferable to adopt a more general calibration method that allows to adopt one "universal" response function to all SiPMs, instead of measuring the individual response function for every SiPM. This is possible by making use of the light yield information for each individual calorimeter cell, which expresses the amount of light seen by one cell for a given energy. The light yield is used to rescale the energy axis of the "universal" response function in order to adapt it to each SiPM.

In the following, the calibration procedure is explained in more detail. Furthermore, the procedure to extract the "universal" response function is discussed. This requires a calibrated light system as "energy" source, and a controlled and stable environment for the read-out system. Finally, the method to extract the response function for all calorimeter cells in the physics prototype is presented. It will mainly serve for monitoring the applicability of the "universal" curve to all SiPMs.

6.1 Calibration Procedure

To calibrate the SiPMs requires to correct for their non-linear response. This can be done by applying the response function (f_{resp}), which translates the number of fired pixels into the number of photo-electrons created in the SiPM:

$$N_{\text{ph.e.}} = f_{\text{resp}}(N_{\text{pixel}}) \ . \tag{6.1}$$

As mentioned above, this "universal"response function has to be applied to all SiPMs. Therefore, a correction for the different light yields (LY), where light yield is defined as the number of photo-electrons released in a SiPM by one MIP passing the scintillator tile, is necessary. Given the preamplification system described in Chapter 4.1, the amplitude recorded by the ADC is proportional to the charge collected by the SiPM. Thus, the light yield is defined as:

$$LY = f_{\text{resp}} \left(\frac{A_{\text{MIP}}}{A^{i+1}_{\text{pix}} - A^{i}_{\text{pix}}} \right) = f_{\text{resp}} \left(\frac{A_{\text{MIP}}}{G_{\text{pix}}} \right) \ , \tag{6.2}$$

where A_{MIP} is the measured amplitude corresponding to one MIP passing the scintillator tile and A^{i}_{pix} is the amplitude of the i-th fired pixel. The response function f_{resp} transforms the ratio $A_{\text{MIP}}/G_{\text{pix}}$ expressed in pixel per MIP into the corresponding ratio in terms of photo-electrons per MIP.

The determination of the light yield implies the knowledge of the SiPM gain. It is defined as the distance between neighbouring peaks in the low light intensity SiPM spectra:

$$G_{\text{pix}} = A^{i+1}_{\text{pix}} - A^{i}_{\text{pix}} \ , \tag{6.3}$$

All these ingredients are combined to calibrate the SiPM signal according to:

$$E = f_{\text{resp}} \left(\frac{A}{G_{\text{pix}}} \right) \cdot \frac{1}{LY} \cdot E_{\text{MIP}} = N_{\text{MIP}} \cdot E_{\text{MIP}} \ , \tag{6.4}$$

where the measured amplitude A is divided by the gain, which transforms the ADC channels into the number of fired pixels N_{pix}, and corrected with the response function to achieve the number of photo-electrons $N_{\text{ph.e.}}$. The light yield is than used to get the number of MIPs N_{MIP}. Finally the number of MIPs is multiplied by the energy of one MIP E_{MIP}, which is taken from Monte-Carlo simulations and can be verified by data taken during the testbeam run in summer 2006, to obtain the total energy deposited.

The various calibration factors can be obtained from different measurements. The SiPM gain is determined from single photo-electron spectra, as described in the following. In order to measure the light yield in terms of photo-electrons per MIP, a calibrated light source, a beam, or cosmic muons can be used. I will concentrate here on the estimation of the SiPM response function f_{resp} which is essential to correct for the non-linear SiPM behaviour.

The SiPM response function is determined for a small representative sample of SiPMs under controlled conditions with a calibrated light source. This method is described in Section 6.2.1. It is too time consuming to be applied for all SiPMs used in the physics prototype. Thus, the response function of the SiPMs in the physics prototype is determined by a second method explained in Section 6.2.2. This multi-channel measurement with an un-calibrated light source can than be compared to the controlled measurement, as all SiPMs behave similar under the same conditions. The un-calibrated light source used to determine the SiPM response function in the physics prototype, is also used to monitor changes of the SiPMs behaviour over time. This monitoring requires to illuminate the SiPMs at a fixed amplitude (see Section 6.3).

6.2 Measurement of the Response Function

In order to obtain the "universal"response function a small representative fraction of SiPMs is measured in a dedicated setup. This is a short time measurement, and therefore does not require a monitoring of the LED light intensity.

The SiPM response function is measured with the setup shown in Figure 6.1. An LED emitting UV light ($\lambda_{\text{max}} \approx 400$ nm) is pulsed by a pulse generator (PM5770 from Philips) at a fixed high amplitude for ~ 10 ns. The amount of light entering the SiPM is controlled with neutral filters. The LED light is focused by an optical lens and guided through a bundle of 19 clear fibres towards one scintillator tile, which is of the same type as the ones used in the physics prototype (see Figure 4.2(b)). The scintillation light is collected by a wavelength shifting (WLS, see Section 4.1) fibre. One end of the WLS fibre is terminated by a mirror, to ensure as much light as possible is reflected to the SiPM, which is connected to the other end of the fibre.

The SiPM signal is read-out with the same electronics as used in the physics prototype. Thus, it is passed to an ASIC chip, where it is amplified and shaped. A signal from the pulse generator serves as a trigger for the ASIC chip. The signal is then held at its maximum amplitude and processed to a 12-bit ADC that is read-out by a VME based data acquisition.

6.2.1 Controlled Measurement

To extract the SiPM response function requires to cover the complete SiPM working range from 1 photo-electron up to roughly 5000 photo-electrons. To measure the response function in terms of pixels per photo-electrons requires to calibrate the light source in photo-electrons. As shown later on, this can be done with neutral filters. Another ingredient needed to extract the response function is an intercalibration factor, as the ASIC chip is used in two different combinations of preamplification gain and shaping time. Finally, one has to scan the full SiPM range. All these steps are explained in more detail in the following.

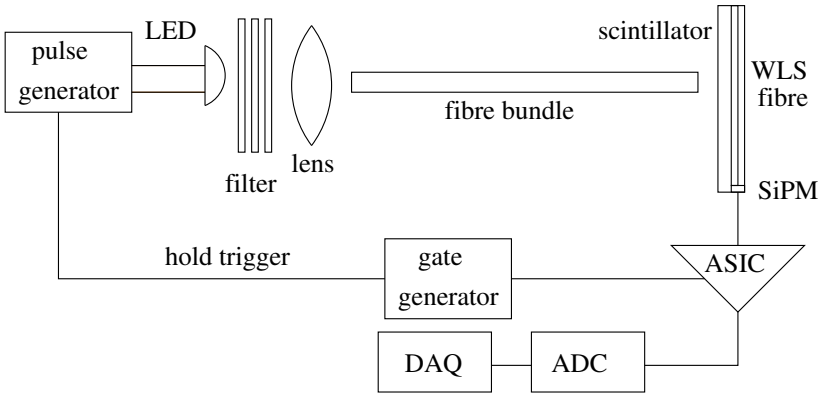

Figure 6.1: Schematic illustration of setup for the measurement of the SiPM response function with neutral filters.

The light source, an LED at a fixed amplitude, is calibrated with neutral filters. The filter calibration is realised with single photo-electron spectra, as they are observed in the SiPMs for low intensity light. One example spectrum is plotted in Figure 6.2(a). The zero peak in the spectrum is the SiPM pedestal peak, the first peak corresponds to one fired pixel, the second to two fired pixels, and so on. These spectra are used

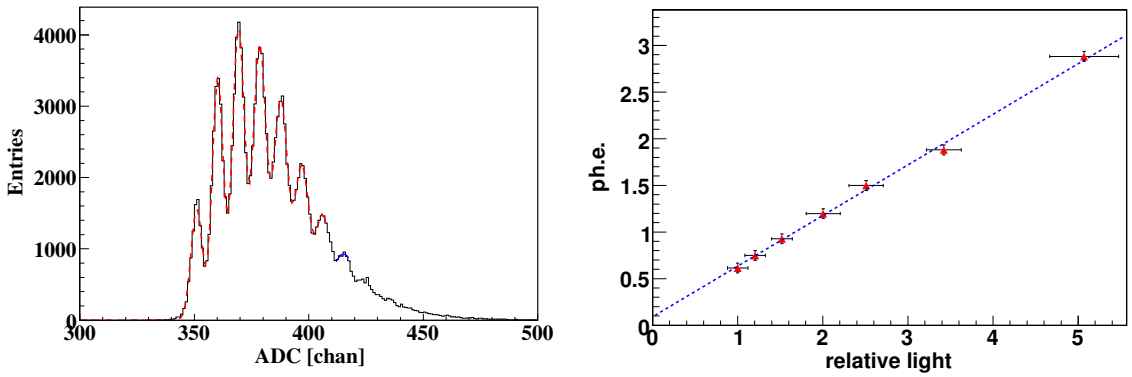

(a) (b)

Figure 6.2: (a) Single photo-electron spectrum taken with a SiPM illuminated by low intensity LED light. (b) Calibration of the neutral filter attenuation in photo-electrons. The x-axis is given in terms of light attenuation of the filters, normalised to the darkest filter.

to convert ADC channels into the corresponding number of fired pixels, and thus to determine the SiPM gain. To obtain the peak positions, a multi-Gauss fit over several

peaks in the spectrum is made.

The pedestal value needed as a starting point for the multi-Gauss fit is extracted from an extra run (Figure 6.3(a)). It is measured under the same conditions as used for the rest of the SiPM response function. A black filter blocks the complete LED light from the SiPM. The long tail to the right is a convolution of dark-rate, i.e. some pixels fire without light, and inter-pixel crosstalk, i.e. a fired pixel can fire a neighbouring pixel. Therefore, it differs from the pedestal shape of other photodetectors, e.g. photomultiplier tubes, whose pedestals are from electronic noise only. The impact of electronic noise on the SiPM pedestal can be measured by biasing the SiPM below breakdown voltage, as shown in Figure 6.3(b).

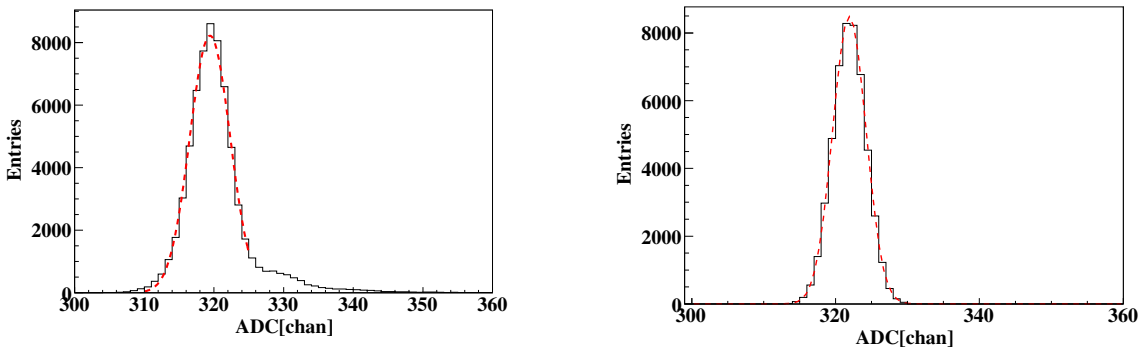

(a) (b)

Figure 6.3: (a) SiPM pedestal showing a long tail due to dark-rate and crosstalk. (b) Contribution from electronic noise to the SiPM pedestal.

The pedestal position is fitted with a Gauss function:

$$f_0(x) = a_0 \cdot \exp\left\{-\frac{1}{2}\left(\frac{x-b_0}{c_0}\right)^2\right\} \ ,$$

where x is the continuous equivalent to the discrete number of ADC channels. All following peaks in the single photo-electron spectra are also fitted with a sum of Gauss functions:

$$F(x) = \sum_{i=1}^{N_{\text{peaks}}} f_i(x) = \sum_{i=1}^{N_{\text{peaks}}} a_i \cdot \exp\left\{-\frac{1}{2}\left(\frac{x-b_i}{c_i}\right)^2\right\} \ ,$$

where N_{peaks} is the total number of peaks in the fitted single photo-electron spectrum. The distance between two following Gauss mean values is the SiPM gain, as defined in Equation 6.3.

The number of photo-electrons is not directly correlated to the number of fired pixels, as one photon can fire more than one pixel due to crosstalk between neighbouring pixels. It is calculated by Poisson statistics as the integral over the spectrum, which is the number of entries N_{entries} in the histogram, with respect to the integral over the pedestal peak:

$$N_{\text{ph.e.}} = \ln\left(\frac{N_{\text{entries}}}{\int f_0(x)\mathrm{dx}}\right) \tag{6.5}$$

The neutral filters can then be translated into the corresponding number of photo-electrons (Figure 6.2(b)). A linear fit on the calibration of the filter attenuation is used to calculate the number of photo-electrons for data points at higher light intensities, where the single photo-electrons cannot be observed directly anymore:

$$N_{\text{ph.e.}} = a \cdot \frac{1}{A_{\text{filter}}} + b \ , \tag{6.6}$$

where the attenuation of the neutral filters A_{filter} is given relative to the light intensity without filters, i.e. the attenuation without filters is one. The offset b is close to zero, and is neglected (in Figure 6.2(b): $a = 0.55 \pm 0.02$ and $b = 0.08 \pm 0.05$).

The error on the number of photo-electrons is a convolution of the error on the neutral filter calibration and the error on the slope of the linear fit:

$$\sigma_{N_{\text{ph.e.}}} = N_{\text{ph.e.}} \cdot \sqrt{\left(\frac{\sigma_{A_{\text{filter}}}}{A_{\text{filter}}}\right)^2 + \left(\frac{\sigma_a}{a}\right)^2} \ , \tag{6.7}$$

where $\sigma_a \sim 4\%$ is the dominating error.

As the SiPM gain is determined in calibration mode and the upper part of the response function is taken in physics mode (see Section 4.1), an intercalibration between these two modes is necessary. This factor κ_{SiPM} transforms the SiPM gain G_{pix}, which is determined as ADC channels per pixel in calibration mode, into the corresponding value in physics mode. One point of the curve has to be taken in both calibration and physics mode. The ratio of the measured signals is the intercalibration factor, that is applied to all data taken in physics mode. For data taken in calibration mode κ_{SiPM} is one.

The number of fired pixels is calculated from the histogram's mean value:

$$N_{\text{pix}} = \frac{A_{\text{cor}}}{G_{\text{pix}}} \cdot \kappa_{\text{SiPM}} \ , \tag{6.8}$$

where $A_{\text{cor}} = A_{\text{SiPM}} - A_{\text{pedestal}}$ is the pedestal subtracted SiPM signal.

The error on the number of fired pixels is dominated by the uncertainty of the gain determination.

$$\sigma_{N_{\text{pix}}} = N_{\text{pix}} \cdot \sqrt{\left(\frac{\sigma_{A_{\text{cor}}}}{A_{\text{cor}}}\right)^2 + \left(\frac{\sigma_{G_{\text{pix}}}}{G_{\text{pix}}}\right)^2 + \left(\frac{\sigma_{\kappa_{\text{SiPM}}}}{\kappa_{\text{SiPM}}}\right)^2} \ , \tag{6.9}$$

where $\sigma_{G_{\text{pix}}} \sim 2\%$.

Using the method described in this section, the saturation curve for one SiPM is measured six times. The results are plotted in Figure 6.4. In Figure 6.4(a) the saturation

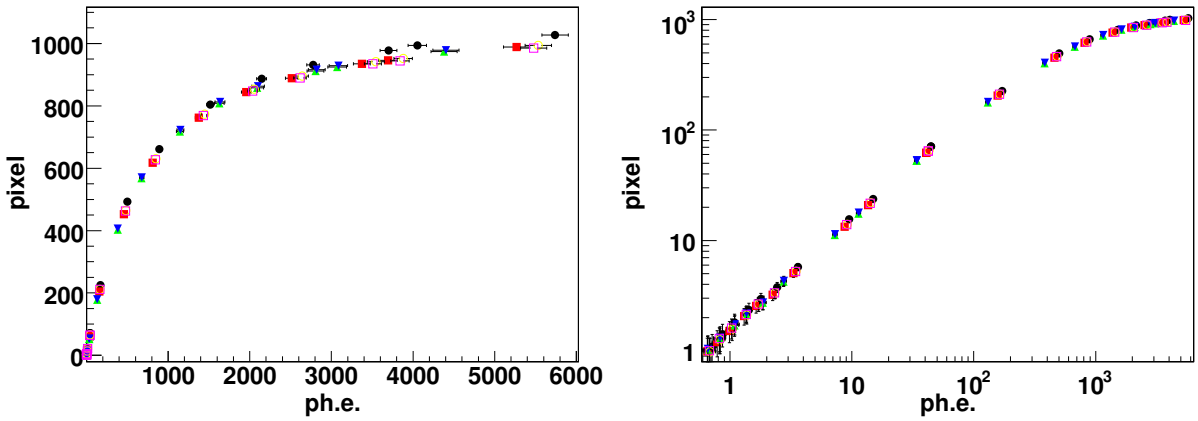

(a) (b)

Figure 6.4: 6 repeated measurements of the response function for one SiPM: (a) in linear and (b) in double logarithmic scale.

of this SiPM can be observed at roughly 1000 pixels, as expected. The linear part of the curve can be appreciated in the double logarithmic scale plotted in Figure 6.4(b). In this representation one can also see the crosstalk effect, as more than one pixel is measured for one photo-electron. For this particular SiPM 1 photo-electron corresponds to 1.6 ± 0.4 pixels. This corresponds to a crosstalk of $(60 \pm 40)\%$ for one photo-electron. This agrees with the expected value of 30% [31]. The huge error on the crosstalk determination reflects the uncertainty of the photo-electron estimation and the reproducibility of this measurement for small light intensities.

The more pixels fire, the smaller is the probability to fire neighbouring pixels, because it becomes more probable that they did already fire due to light. The error on the pixel determination is dominated by the uncertainty of the gain estimation, which is $\sim 2\%$. The error of $\sim 4\%$ on the photo-electron determination is dominated by the error on the slope of the linear fit.

The measured saturation curve looks like expected. It can now be compared to simulations and used to parametrise the SiPM response function. The errors on the curve can be further reduced by a more precise filter calibration and more data points in the low intensity light region, to minimise the error on the linear fit.

6.2.2 Multi-Channel Measurement

The response functions of about 8000 SiPMs have to be measured and monitored. Up to now this was only tested for a small fraction of channels (3 LEDs illuminating 54 SiPMs) to prove the working principle. The setup differs from the controlled measurement. A data acquisition (DAQ) controls the LED voltage pulse width and amplitude of all 500 LEDs needed to monitor the physics prototype. For the results presented here two small LED driver prototypes, each able to pulse two LEDs, were used. The light is distributed to 18 SiPMs and one PIN photodiode through clear fibres, as explained in Chapter 5.1. The signal of 18 SiPMs is passed to one ASIC chip, the same as in the controlled measurement, where they are amplified, shaped and multiplexed. The signal from 12 ASIC chips are forwarded to one connector of the CALICE Readout Card (CRC), containing 16-bit ADCs, with 8 connectors in total (see Chapter 4.1).

The steps for the simultaneous measurement of many response functions, are almost the same as for the controlled one. A PIN photodiode signal is used as linear reference for the light intensity. Three PIN photodiode signals are preamplified with two prototypes of the PIN photodiode preamplifier before they are passed on to the same type of read-out electronics as used for the SiPMs and follow the SiPM signal chain. As the PIN photodiode is working in its own mode, an additional intercalibration factor has to be determined. Data are taken with a special scan, increasing the LED light, covering pedestal and single photo-electron spectra in calibration mode, as well as the complete LED range from zero light to the LED maximum light output in physics mode.

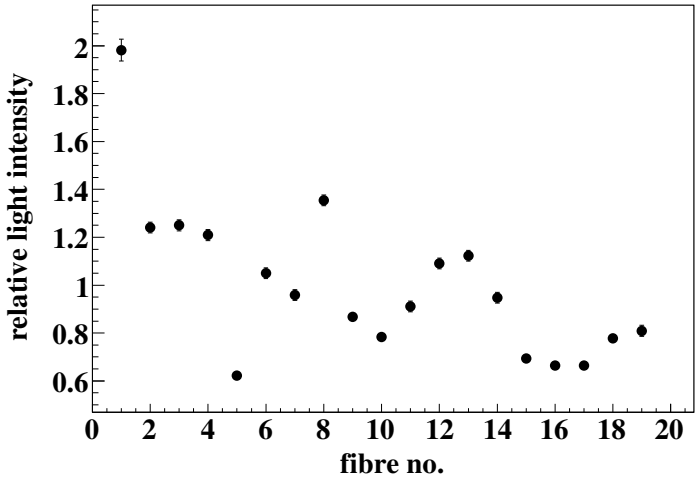

Figure 6.5: Light spread in a bundle with a thicker centre fibre, normalised to the mean value.

To match the working ranges of SiPMs and PIN photodiodes, the LED surface is darkened, except for a small hole in the middle. In this way the PIN photodiodes get a

signal in a range where the SiPMs can be operated in the high-gain calibration mode. With this modification it is possible to measure the lower part of the response function, but only ~ 600 out of 1156 pixels are fired. This mismatch of the two ranges can be improved with an increase of the central fibre diameter fibre from the currently used 0.75 mm to 1.0 mm. This reduces the discrepancy by a factor of 2 (see Figure 6.5). First tests look promising, but it is technically more challenging than to make a bundle of fibres with equal diameter.

To extract the SiPM response function in the physics prototype requires almost the same ingredients as in the controlled measurement, which is described in Section 6.2.1. The gain is again determined by fitting single photo-electron spectra with a multi-Gauss fit, as described in Section 6.2.1. Figure 6.6 shows the distribution of the gain determined for 54 SiPMs. The mean value is (252 ± 34) [chan/pix] with a root mean square (RMS) of (30 ± 4) [chan/pix]. This corresponds to a spread of 12%.

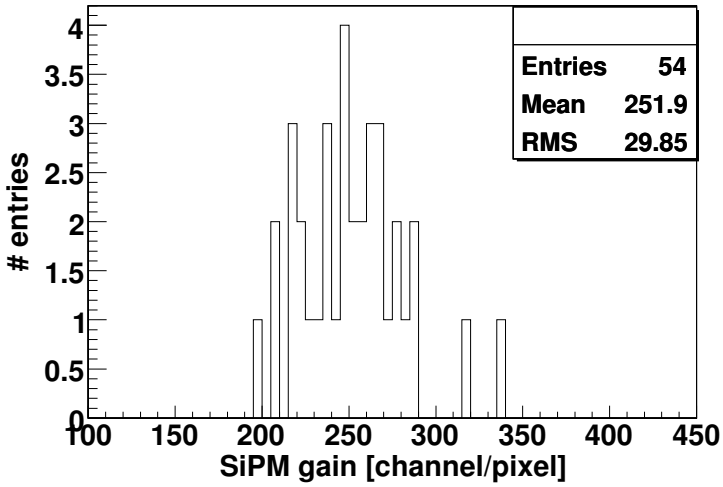

Figure 6.6: Gain variation of 54 SiPMs illuminated by 3 LEDs.

The intercalibration factor κ_{SiPM} between calibration and physics mode depends on the SiPM resistor (Figure 6.8). The mean value for SiPMs with $1-2$ MΩ resistors is (8.0 ± 0.1) [$\mathrm{chan_{calib}}/\mathrm{chan_{phys}}$] with an RMS of (0.4 ± 0.2) [$\mathrm{chan_{calib}}/\mathrm{chan_{phys}}$]. All SiPMs with resistors > 8 MΩ have a mean value of (11.4 ± 0.1) [$\mathrm{chan_{calib}}/\mathrm{chan_{phys}}$] with an RMS of (0.4 ± 0.2) [$\mathrm{chan_{calib}}/\mathrm{chan_{phys}}$]. The observed 5% spread of the intercalibration factors for SiPMs with similar resistors match the spread in gain of the ASIC chips, that are selected to be within 5% [32]. The individual intercalibration factor of every channel is measured and applied to determine the particular response function for each SiPM.

The different intercalibration factors originate from different SiPM signal shapes for SiPMs with different resistors. The fast part of the SiPM signal is always followed by

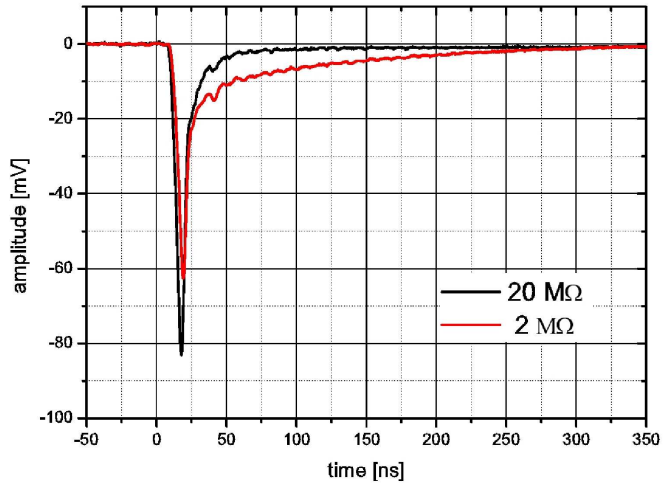

Figure 6.7: Oscilloscope picture of two SiPM signals. One from a SiPM with 2 MΩ and the other from a SiPM with 20 MΩ quenching resistor.

a long tail. The ratio between these two parts varies for different resistors, because the time constant of the signal decay depends on the resistor. This is illustrated in Figure 6.7, where the black curve is the fast decaying signal of a SiPM with 20 MΩ resistor and the red curve is the signal of a SiPM with 2 MΩ resistor with longer tail, taken with an oscilloscope. The larger the resistor, the faster the discharge time of the signal. This re-charge is governed by $\exp\{-t/\tau\}$, where $\tau = R_{\text{quench}} \cdot C_{\text{pix}}$ is the pixel recovery time (see Section 4.2). The re-charge time is longer for bigger resistors. As the area under the tail that follows the fast discharge signal is always the same, it is higher and shorter for SiPMs with smaller resistors, and narrower and longer for SiPMs with bigger resistors [33]. The read-out electronics integrate over a bigger part of the shaped signal for high resistivity SiPMs in the calibration mode with 40 ns integrating time (see Section 4.1), and the ratio between a calibration mode and a physics mode signal is bigger.

The spread amongst the 18 curves obtained with the monitoring system described in Chapter 5 is shown in Figure 6.9. The light intensities seen by the SiPMs are different due to the fibre system and the spread in light yield. Plotted are the signals of 18 SiPMs illuminated by one LED versus the signal of the PIN photodiode, that is monitoring this LED, in ADC channels(Figure 6.9(a)). The errors on these curves are statistical only. As shown in Chapter 5.1 there is a factor two of spread in light intensity between brightest and dimmest fibre, amongst the channels belonging to one LED originating from the light distribution system. In addition, the scintillator tiles have a 10% spread

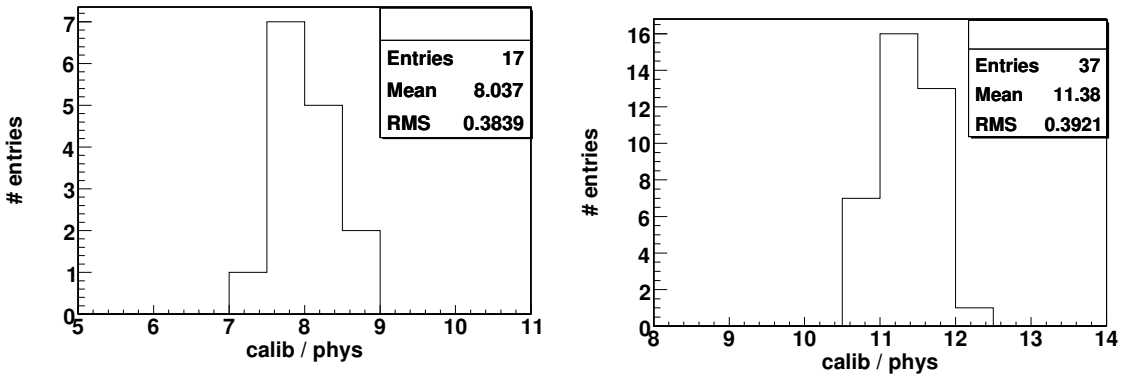

(a) (b)

Figure 6.8: Spread of the intercalibration factor between calibration and physics mode for (a) SiPMs with $1-2$ $M\Omega$ quenching resistor, (b) SiPMs with > 8 $M\Omega$ quenching resistors.

in light yield [11] and the darkening of the LEDs introduced inhomogeneities, too. The overall spread results in a factor ~ 4.

This curves cannot directly be compared to the SiPM response function as it is given in Chapter 6.2.1, as the x-axis is not calibrated in photo-electrons. This would require to measure a PIN photodiode signal at the one MIP level, because we can only correct for the SiPM crosstalk, which is a non-linear characteristic, at this point. With this correction the number of fired SiPM pixels can be translated into the number of incident photo-electrons, that can than be used to calibrate the PIN photodiode at this point. As the PIN photodiode signal is linear, this is sufficient to calibrate the x-axis in photo-electrons.

However, we can still use the PIN photodiode signal to correct for the light intensity spread between the different SiPMs. Assuming that all SiPMs give the same signal at the same light intensity, the SiPM signals are normalised to one common light intensity, in the linear range of the SiPM signals, where saturation effects are negligible, at a certain amount of light in the PIN photodiode. This is done in Figure 6.9(b).

The y-axis of these curves reflects the SiPM signal (S_{SiPM}). It is given in pixels, to correct for the gain spread among the SiPMs:

$$S_{\mathrm{SiPM}} = A_{\mathrm{SiPM}}/G_{\mathrm{pix}} \cdot \kappa_{\mathrm{SiPM}} \ , \tag{6.10}$$

where A_{SiPM} is the silicon photomultiplier amplitude in ADC channels measured in physics mode, G_{pix} is the SiPM gain in terms of ADC channels per pixel determined in calibration mode and κ_{SiPM} is the intercalibration factor between physics and calibration mode, as already described in Section 6.2.1.

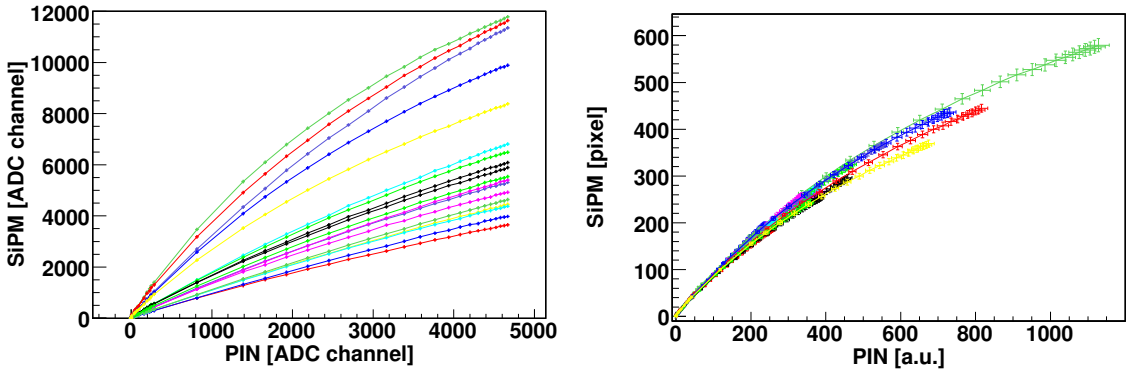

(a) (b)

Figure 6.9: Response of 18 SiPMs illuminated by one LED: (a) SiPMs in ADC channels versus PIN in ADC channels, (b) corrected for the different SiPM gains and the light spread. The number of fired pixels is plotted versus the light intensity measured by the PIN photodiode in arbitrary units.

The x-axis is calculated from the PIN photodiode amplitude (A_{PIN}):

$$S_{\mathrm{PIN}} = A_{\mathrm{PIN}} \cdot F_{\mathrm{light}} \ , \tag{6.11}$$

where F_{light} is a calibration factor to compensate for the different light intensities seen by the SiPM due to the spread in the fibre system, the spread in light yield and the SiPM gain variation.

The spread between the curves in Figure 6.9 can be reduced to 11%, by adjusting them to one common point. This spread reflects the different number of active pixels on each SiPM, the spread in crosstalk among the different SiPMs and the calibration errors on the gain determination. They are not directly comparable to the SiPM response functions determined in Section 6.2, as the x-axis is not calibrated in photo-electrons. Instead these curves are used to monitor changes of the SiPM behaviour over time.

6.3 Monitoring the Time Stability

In this section the monitoring of the SiPM response in the physics prototype is described. The SiPM behaviour may change over time, e.g. due to temperature fluctuations. Thus, their signal has to be monitored continuously. This longterm measurement has to be monitored by a stable photodetector, to correct for changes of the LED light intensity during the measurement.

The monitoring of the SiPMs in the physics prototype is part of a redundant system to check the stability of the detector. A reference light pulse of the LED system is complemented by a slow control system that measures temperature, SiPM bias voltage and SiPM current. Another possibility to observe temperature changes is the SiPM gain determination, as the SiPM gain changes with temperature and bias voltage (see Table 4.2).

To reduce the number of monitoring events, a detailed response function scan is only performed from time to time. In between the SiPMs are monitored at a fixed light intensity. It would have been nice to monitor at the MIP level, where the SiPM behave quite linear, and one would be able to compare the monitoring data directly to cosmic data. But as the PIN photodiodes are not sensitive to this light intensities, we had to monitor at more than 10 MIPs.

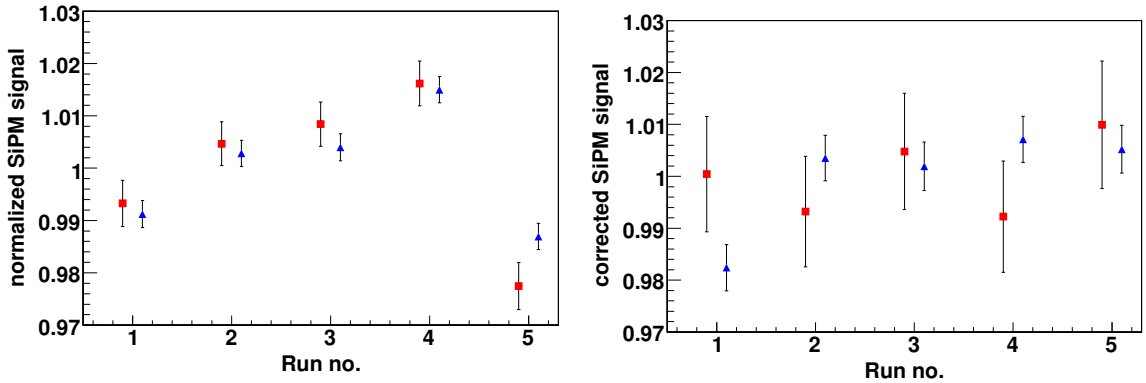

(a) (b)

Figure 6.10: 5 repeated measurements to monitor the SiPM behaviour over time. (a) Uncorrected SiPM signal for low (red squares), and medium (blue triangles) light intensities. (b) The same points corrected for fluctuations in the LED light intensity by a PIN photodiode.

The signal of one SiPM is measured once a day during one week in between cosmic data taking. This intermediate monitoring will also be used during the testbeam period in summer 2006. In order to quantify the SiPM behaviour over time, the SiPM signal development at low (red squares), and medium (blue triangles) LED intensity is plotted versus run number in Figure 6.10(a). The runs were taken between January 3 and January 8, 2006. The SiPM signal is normalised to the mean value.

The uncorrected SiPM signals indicate a trend in time. A jump of the SiPM signal in the last run could result from temperature variations. The SiPM signals that are corrected by the PIN photodiode, as plotted in Figure 6.10(b) do not show this trend.

The jump in the last run is no longer visible, thus it has to be due to fluctuations of the LED light intensity. This points to the necessity of monitoring the LED light intensity with a PIN photodiode for a long time measurement. The errors in this plot are bigger than they are for the uncorrected signals, because the error of the PIN photodiode signal has to be taken into account for the corrected values. Hence, the highest precision can be achieved for higher light intensities (blue triangles), where the PIN photodiode gets enough light and the errors on its signal become smaller.

With the PIN photodiode corrected LED light, the SiPM signal can be monitored with $\sim 1\%$ precision at low light intensity. The ambitious goal of this monitoring system is achieved for the tested sample of SiPMs. The accuracy of the monitoring could even be further improved by monitoring at higher light intensities.

Chapter 7

Summary and Outlook

To investigate hadronic shower models and to test a new semiconductor based photodetector, a physics prototype of an analogue hadronic calorimeter for the *International Linear Collider*, is currently build at the *Deutsches Elektronen-Synchrotron* within the collaboration for a *CAlorimeter for the LInear Collider Experiment*. This prototype is realised as a high granular scintillator-steel sandwich calorimeter read-out with a novel pixel photodetector device called silicon photomultiplier.

This thesis presents the successful testing and optimisation of the calibration and monitoring system for this physics prototype, as well as a measurement of the non-linear response function of these SiPMs. In addition the stability of the SiPM response over time is investigated.

The response function of the silicon photomultipliers is determined with calibrated neutral filters. It will be used to correct for the non-linear SiPM behaviour and to get a deeper understanding of this new read-out technology.

The light cone homogeneity from the LEDs used to determine the response function, is measured to be better than a factor 1.5. Together with the light distribution system the light intensity spread is less than a factor two. This is sufficient to obtain single photo-electron spectra, with one LED voltage setting per LED, reducing the time needed for calibration and monitoring to a minimum, which allows more time to take physics data. Single photo-electron spectra are used to determine the SiPM gain for the first six completed layers of the physics prototype.

It is demonstrated that the SiPM response can be monitored at a fixed LED light intensity with 1% precision, after correction of the LED light intensity with a PIN photodiode. This proofs that the principle of the monitoring system as foreseen for the physics prototype is working. In addition the complete SiPM working range, from 1 to 1156 fired pixels, can be tested with the calibration and monitoring system. The PIN photodiode is necessary for both measurements, to disentangle changes of the SiPM signal from fluctuations in the LED light intensity.

The assembly of the physics prototype has to be finished. A combined testbeam run with the prototypes of the ECAL and the Tail-Catcher will be done in summer 2006. It will serve as test of the chosen technologies: the silicon photomultipliers as well as the read-out electronics and the calibration and monitoring system. Furthermore, the data taken in this testbeam run will help to understand hadronic shower development, which will improve detector simulations. The experience gained with the physics prototype will be considered in the design and realisation of a prototype that is scalable to a calorimeter that can be used within a detector at the ILC.

Bibliography

[1] The LEP Collaborations: A combination of preliminary electroweak measurements and constraints on the standard model, arXiv:hep-ex/0412015.

[2] The LEP Electroweak Working Group (LEP EWWG): http://lepewwg.web.cern.ch/LEPEWWG/x

[3] G. Altarelli: Precision Electroweak Test of the Standard Model, CERN-PH-TH/2004-067 (2004).

[4] The SiD group: SiD Detector Outline Document, April 2006

[5] Stanford Linear Accelerator Center, www-sid.slac.stanford.edu

[6] The LDC group: Large Detector Concept Outline Document, April 2006.

[7] Large Detector Concept home page: www.ilcldc.org

[8] The GLD Concept Study Group: GLD Detector Outline Document, March 2006.

[9] Japanese Accelerator Center KEK, http://ilcphys.kek.jp/gld/

[10] Description of the Fourth Concept Detector (4th) v 0.2, Nov. 2005.

[11] Linear Collider Detector R&D, DESY PRC-R&D 2005.

[12] The CALICE collaboration: CAlorimeter for a LInear Collider with Electrons, http://polywww.in2p3.fr/flc/calice.html

[13] J. C. Brient: The Calorimetry at the future e^+e^- linear collider, February 2002.

[14] TESLA - The Superconducting Electron-Positron Linear Collider with an Integrated X-Ray Laser Laboratory, Technical Design Report, DESY 2001-011(2001).

[15] J. C. Brient: Improving the Jet Reconstruction with the Particle Flow Method; an Introduction, polywww.in2p3.fr/ brient/ CALOR04/ParticleFlow-Brient.pdf

[16] F. Sauli: Development and applications of gas electron multiplier detectors, Nucl. Instrum. Meth. A **505** (2003) 195.

[17] Y. Giomataris et al: Micromegas: a High Granularity Position Sensitive Gaseous Detector for High Particle Flux Environments, Nucl. Instrum. Meth. A **386:531** (1996).

[18] Fermi National Accelerator Laboratory, http://ilc.fnal.gov/detector/rd/detrd.html

[19] A. Raspereza: Two Particle Separation with Tile HCAL, LC Workshop 2004.

[20] Forschung mit Lepton Collidern, http://www-flc.desy.de/hcal/tilehcal

[21] M. Thomson: Concepts, Calorimetry and PFA, Snowmass 2005.

[22] in preparation, B. Lutz: Diplomarbeit, to be published in Hamburg 2006.

[23] R. Wigmans: Calorimetry - Energy Measurement in Particle Physics, Oxford University Press (2000).

[24] Particle Data Group, S. Eidelman et al: Physics Letters B592, 1 (2004), http://pdg.lbl.gov.

[25] F. Sefkow: Performance Goals and Design Considerations for a Linear Collider Calorimeter, LC-DET-2004-022 (2004).

[26] V. Korbel, V. Morgunov: Calibration and Monitoring of the TESLA Tile Hadron Calorimeter, LC-DET-2001-051 (2001).

[27] M. Groll: Dedicated Front-end Electronics for an ILC Prototype Hadronic Calorimeter with SiPM Read-out, October 2005

[28] P. Buzhan et al: An advanced study of Silicon Photomultiplier, ICFA Instrumentation Bulletin.

[29] V. Andreev et al: A High Granularity Scintillator Hadronic-Calorimeter with SiPM Readout for a Linear Collider Detector, LC-DET-2004-027 (2004).

[30] E. Garutti: Calibration and Monitoring of the analog HCAL Prototype, 2005 International Collider Workshop - Stanford.

[31] V. Popov: Method for calibration of the tile HCAL with silicon photomultiplier as a photodetector (proposal), LC-DET-2003-092 (2003).

[32] E. Garutti: private communication.

[33] F. Sefkow: private communication.

Danksagung

Ich bedanke mich bei der Gruppe FLC für die schöne Zeit.

Insbesondere bei Rolf-Dieter Heuer für die Möglichkeit in seiner Forschungsgruppe arbeiten zu dürfen. Mein Dank gebührt auch Götz Heinzelmann für die Zweitkorrektur.

Ebenfalls bedanken möchte ich mich bei Ties Behnke und Felix Sefkow. Desweiteren danke ich Erika Garutti und Sebastian Schätzel für die gute Betreuung.

Bei Hendrik Meyer und Benjamin Lutz bedanke ich mich für die nette Zusammenarbeit, sowie bei Marius Groll und Thomas Krämer fürs Korrekturlesen.

Für die technische Unterstützung bedanke ich mich bei Ivo Polak, Karsten Gadow, Sven Karstensen, Gerd Fally und Petr Smirnov. Ramona Matthes danke ich für ihre Hilfe bei Verwaltungsangelegenheiten.

Ganz besonders danken möchte ich meinem Freund Filip Schmidt-Petersen, der wáhrend meines gesamtem Studiums zu mir gehalten hat.

Erklärung

Hiermit versichere ich, die vorliegende Arbeit selbständig und nur unter Verwendung der angegebenen Quellen und Hilfsmittel verfasst zu haben. Ich gestatte die Veröffentlichung dieser Arbeit.